From soft and hard particle simulations to continuum theory for granular flows

S. Luding, N. Rivas, T. Weinhart

Multi-Scale Mechanics, Faculty of Engineering Technology (ET), MESA+, University of Twente, Enschede, The Netherlands

One challenge of today's research is the realistic simulation of disordered many particle systems in static and dynamic/flow situations. Examples are particulate and granular materials like sand, powders, ceramics or composites, with applications in particle-technology and geo-technical/physical systems. The inhomogeneous micro-structure of such materials makes it very difficult to model them with continuum methods, which typically assume homogeneity on the microscale and scale separation between the constituents and the macroscopic fields. As an alternative, discrete particle methods can be applied, since they intrinsically take the micro-structure into account. The ultimate challenge is to bridge the gap between both approaches by using particle-simulations to obtain appropriate constitutive relations for continuum theories, and work with those on the macro-scale. Here, soft and hard particle simulation methods are introduced as well as the micro-macro transition to obtain the continuum fields from the particle data. Two application examples discussed in detail concern the flow of particle down an incline, as relevant for geo-flows, as well as a vibrated granular system as relevant for highly agitated transport or conveying processes.

1 Introduction

Most general materials have inhomogeneous micro-structures such as powders, sands, and even geo-materials. In such discrete, particulate, granular systems the particles can be complex, non-spherical, and consist of different materials. The idealized constituents we focus on in the following are spherical, polydisperse, elasto-plastic, adhesive, and frictional objects.

One approach towards the microscopic understanding of such macroscopic particulate material behavior [HHL98, Kis01, HW04] is the discrete modeling of particles. Soft and hard particle methods are discussed here, while other particle methods like contact

dynamics (CD) are discussed in Ref. [Rad]. The method of particle simulations, and the practical aspects are also addressed in other lectures and practicals [CR, TWT], where more details on contact-models [Mar] are as important as the careful sample preparation [CR], and methods to model and interpret geotechnical experiments [DS, TML].

Even though millions of particles can be simulated, the possible size of such a particle system is in general too small to regard it as macroscopic. Therefore, methods and tools to perform a so-called micro-macro transition [VDE$^+$01, PL01, KBG49] are discussed. "Microscopic" particle simulations can be used to derive macroscopic constitutive relations, as needed to describe the material within the framework of continuum theory, on the scales of large industrial unit-operations and natural/geotechnical phenomena like avalanches or landslides.

In idealized granular materials, when the particle properties and interaction laws are defined, the equations of motion can be integrated in time. The collective behavior of dissipative many-particle systems can be studied in static and dynamic situations as well. For example, from particle simulations one can extract the pressure of the system as a function of density. This "equation of state" can then be used for the macroscopic description of dynamic materials, which can be viewed as a compressible, non-Newtonian complex fluid [LLH01], including fluid-solid phase transitions and energy dissipation terms.

Several techniques have been used to calculate the continuum fields from steady state flow situations, see [LAM11] and references therein. The stress tensor is of particular interest for the momentum balance equations: previous techniques include the Irvin-Kirkwood's approach [IK50] or the method of planes [TED95]. Here, we use the coarse-graining approach as originally described in Ref. [Bab97, Gol10, WTLB12a, WLT13], and as also presented in the paper by Thornton [TWT]. It has the following advantages as compared to other methods: (*i*) the resulting fields automatically satisfy exactly the equations of continuum mechanics, also near boundaries or in mixtures, if corrected as proposed in [WTLB12a, WLT13], (*ii*) it is not assumed that the particles are spherical (but a single point of contact is required); and, (*iii*) the results are valid even for single particles and at one moment in time, as no ensemble averaging is required to satisfy the mass and momentum balance.

In the following, two particle simulation methods are introduced. The first is the so-called soft sphere Discrete Element Method (DEM), which is also often referred to as Molecular Dynamics (MD), as described in Section 2. It is straightforward to implement a solver for the equations of motion for a system of many interacting particles [AT87, Rap95]. For DEM, both normal and tangential interactions, like friction, are discussed for spherical particles. The second method is the so-called Event-Driven (ED) simulation, discussed in Section 3, which is conceptually different from DEM, since collisions are dealt with via a collision matrix that in one step determines the momentum change on physical grounds. For the sake of brevity, the ED method is only discussed for smooth (that is, frictionless) spherical particles. Furthermore, a method to relate the soft and hard particle methods is provided in Section 4. For more

details on ED simulations see Ref. [Lud09] and references therein. To illustrate the micro-macro transition, the density, velocity and stress for a system of soft or hard spheres is defined in Section 5 by means of coarse graining, also referred to as the "micro-macro transition". Two examples are discussed in detail: First, chute flow in Section 6, where the above-described simulation methods can be applied for quasi-static, slow and inertial, dynamic systems. Macroscopic quantities are obtained using the micro-macro transition (or coarse graining) methodology introduced in the earlier chapters and all the resulting tensorial fields are discussed in depth, even though most of them are usually neglected in very many application and research studies. Second, the example of vibrated, collisional systems is presented in Section 7, where the two methods DEM and ED can be directly compared. Situations where he methods lead to the same results are presented together with cases where the results are differing.

2 The Soft-Particle Discrete Element Method

The elementary units of granular materials are mesoscopic grains which deform under stress. Since the realistic modeling of the deformations of the particles is much too complicated, we relate the interaction force to the overlap δ of two particles as a first order approximation, see Fig. 1a. Note that the evaluation of the inter-particle forces based on the overlap may not be sufficient to account for the inhomogeneous stress distribution inside the particles, and related multi-contact effects. Consequently, our results presented below are of the same quality as the simplifying assumptions about the pairwise force-overlap relation.

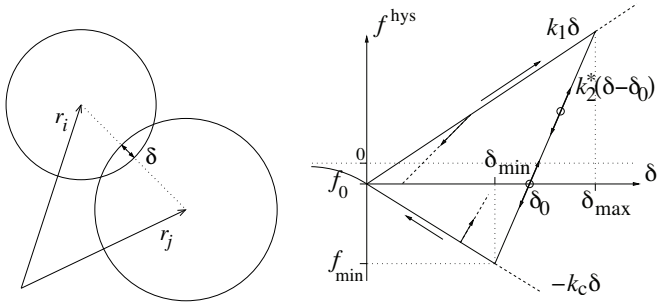

Figure 1: (Left) Two particle contact with overlap δ. (Right) Schematic graph of the piecewise linear, hysteretic, adhesive force-displacement model introduced below in Eq. (6). Note the important non-linearity of contact stiffness with confining stress (previous maximal overlap, $\delta_{\max}$), that manifests in the functional dependence of $k_2^*(\delta_{\max})$, as specified below in Eqs. (7) and (8).

2.1 Equations of Motion

If the total force $\vec{f}_i$ acting on particle i, either due to other particles and boundaries or from external forces, is known, then the problem is reduced to the integration of Newton's equations of motion for the translational and rotational degrees of freedom,

$$m_i \frac{\mathrm{d}^2}{\mathrm{d}t^2}\vec{r}_i = \vec{f}_i + m_i\vec{g}, \quad \text{and} \quad I_i \frac{\mathrm{d}}{\mathrm{d}t}\vec{\omega}_i = \vec{t}_i, \tag{1}$$

with m_i the mass of particle i, $\vec{r}_i$ its position, $\vec{f}_i = \sum_c \vec{f}_i^c$ the total force acting on it due to contacts with other particles or with the walls, $\vec{g}$ the acceleration due to volume forces like gravity, I_i the spherical particle's moment of inertia, $\vec{\omega}_i$ its angular velocity and $\vec{t}_i = \sum_c \left(\vec{l}_i^c \times \vec{f}_i^c + \vec{q}_i^c\right)$ the total torque, where $\vec{q}_i^c$ are torques/couples at contacts other than the torques due to the tangential force, e.g., due to rolling and torsion, and $\vec{l}_i^c$ the vector from the particle's centre of mass to the contact point.

The equations of motion are thus a system of $\mathcal{D} + \mathcal{D}(\mathcal{D}-1)/2$ coupled ordinary differential equations to be solved in $\mathcal{D}$ dimensions. The solution of such equations is straightforward, using numerical integration tools such as the ones nicely described in textbooks [AT87, Rap95]. The typically short-ranged interactions in granular media allow for further optimizations by using linked-cell spatial structures or alternative methods [AT87, Rap95, KOL14] in order to make the search for colliding particles more efficient. In the case of long-range interactions, (e.g. charged particles with Coulomb interaction, or objects in space with self-gravity) this is not possible anymore, so that more advanced methods for optimization have to be applied. Here we restrict ourselves to short-range interactions.

Specifically, two spherical particles i and j, with radii a_i and a_j, respectively, interact only if they are in contact, that is, their overlap

$$\delta = (a_i + a_j) - (\vec{r}_i - \vec{r}_j)\cdot\vec{n} \tag{2}$$

is positive, $\delta > 0$, with the unit vector $\vec{n} = \vec{n}_{ij} = (\vec{r}_i - \vec{r}_j)/|\vec{r}_i - \vec{r}_j|$ pointing from j to i. Note the different sign convention used in the contact dynamics (CD) method, where $\delta > 0$ means a separation and not the contact of particles [Rad]. The force on particle i, from particle j, at contact c, can be decomposed into a normal and a tangential part as $\vec{f}^c := \vec{f}_{ij}^c = f^n\vec{n} + f^t\vec{t}$. In the following, we specify $\vec{f}_{ij}^c$ for different models that take into account increasingly complicated grain interactions, see also Ref. [Mar]. We begin by discussing f^n.

2.2 Normal Contact Force Laws

2.2.1 Linear Normal Contact Model

The simplest normal contact force model, which takes into account excluded volume and dissipation, involves a linear repulsive and a linear dissipative force,

$$f^n = k\delta + \gamma_0 v_n \ , \tag{3}$$

with a spring stiffness k, a viscous damping γ_0, and the relative velocity in normal direction $v_n = -\vec{v}_{ij} \cdot \vec{n} = -(\vec{v}_i - \vec{v}_j) \cdot \vec{n} = \dot{\delta}$. This so-called linear spring dashpot model considers the particle interactions as a damped harmonic oscillator. As such, the half-period of a vibration around an equilibrium position can be computed, obtaining a typical response time on the contact level,

$$t_c = \frac{\pi}{\omega} \ , \quad \text{with} \quad \omega = \sqrt{(k/m_{ij}) - \eta_0^2} \ , \tag{4}$$

with the eigenfrequency of the contact ω, the rescaled damping coefficient $\eta_0 = \gamma_0/(2m_{ij})$, and the reduced mass $m_{ij} = m_i m_j/(m_i + m_j)$. From the solution of the velocity at the half period of the oscillation, one also obtains the coefficient of restitution,

$$r = -v_n'/v_n = \exp\left(-\pi\eta_0/\omega\right) = \exp\left(-\eta_0 t_c\right) \ , \tag{5}$$

which quantifies the ratio of relative velocities after (primed) and before (unprimed) the collision. For a deeper discussion of the coefficient of restitution and other, more realistic, non-linear contact models, see e.g. [Lud98, SML15, TCC17] and the papers by Martin [Mar] and Radjai [Rad].

The contact duration in Eq. (4) is also of practical technical importance, since the integration of the equations of motion is stable only if the integration time-step $\Delta t_{\rm DEM}$ is much smaller than t_c. Furthermore, notice that in the extreme case of an overdamped spring, t_c can become very large, and therefore the use of neither too weak nor too strong dissipation is recommended.

2.2.2 Adhesive, Elasto-Plastic Normal Contact Model

Let us now consider a variant of the linear hysteretic spring model [WB86, Lud98, Tom00, Lud08], as an alternative to the frequently used spring-dashpot models. This model is a simple version of some more complicated nonlinear-hysteretic force laws [WB86, ZSS91, STS93], which reflects the fact that plastic deformations take place at the contact point. Overall, the model is meso-scopic [SMSL14], i.e. it describes the collective interactions of a bulk of primary particles that are represented by a meso-particle. The repulsive (hysteretic) force can be written as

$$f^{\rm hys} = \begin{cases} k_1\delta & \text{for loading,} & \text{if } k_2^*(\delta-\delta_0) \geq k_1\delta \\ k_2^*(\delta-\delta_0) & \text{for un/reloading,} & \text{if } k_1\delta > k_2^*(\delta-\delta_0) > -k_c\delta \\ -k_c\delta & \text{for unloading,} & \text{if } -k_c\delta \geq k_2^*(\delta-\delta_0) \end{cases} \ , \tag{6}$$

with $k_2^* \geq k_1 > 0$. The constant k_2^* is determined by the parameter k_2, as explained below. Fig. 1 shows an schematic of the loading and unloading process.

During the initial loading the force increases linearly with the overlap δ, until the maximum overlap $\delta_{\max}$ is reached (which has to be kept in memory as a history parameter). The line with slope k_1 thus defines the maximum force possible for a given δ. During unloading the force drops from its value at $\delta_{\max}$ down to zero at overlap $\delta_0 = (1 - k_1/k_2^*)\delta_{\max}$, on the line with slope k_2^*. Reloading at any instant leads to an increase of the force along this line, until the maximum force is reached; for still increasing δ, the force follows again the line with slope k_1 and $\delta_{\max}$ has to be adjusted accordingly.

Unloading below δ_0 leads to negative, i.e. attractive, forces until the minimum force $-k_c\delta_{\min}$ is reached at the overlap $\delta_{\min} = (k_2^* - k_1)\delta_{\max}/(k_2^* + k_c)$. This minimum force, i.e. the maximum attractive force, is obtained as a function of the model parameters k_1, k_2, k_c, and the history parameter $\delta_{\max}$. Further unloading leads to attractive forces $f^{\rm hys} = -k_c\delta$ on the adhesive branch with slope $-k_c$. The highest possible attractive force, for given k_1 and k_2, is reached for $k_c \to \infty$, so that $f_{\max}^{\rm hys} = -(k_2 - k_1)\delta_{\max}$. Since this would lead to a discontinuity at $\delta = 0$, it is avoided by using finite $k_c \geq 0$.

The lines with slope k_1 and $-k_c$ define the range of possible force values and departure from these lines takes place in the case of unloading and reloading, respectively. Between these two extremes, unloading and reloading follow the same line with slope k_2^*. Possible equilibrium states are indicated as circles in Fig. 1, where the upper and lower circle correspond to pre-stressed states with repulsive and attractive forces, respectively. Small overlap perturbations lead to small force deviations along the line with slope k_2^*, as indicated by the arrows.

Even though a non-linear un-/reloading behavior would be more realistic, we use the piecewise linear model as a compromise, mainly due to a lack of detailed experimental information for better calibrating the model. Only recently, due to nano-indenters and their more reliable force-displacement sensors, experimental data for unloading forces on the contact level between small particles become available. One refinement of the older models involves considering an unloading stiffness k_2^* dependent on the maximum overlap, i.e. the contact force and confining stress [LMM05, Lud08, SMSL14, SML15]. Introducing an additional contact-history parameter, the maximal overlap, $\delta_{\max}^p$, one has

$$k_2^*(\delta_{\max}) = \begin{cases} k_2 & \text{if } \delta_{\max} \geq \delta_{\max}^p \\ k_1 + (k_2 - k_1)\delta_{\max}/\delta_{\max}^* & \text{if } \delta_{\max} < \delta_{\max}^p \end{cases} , \tag{7}$$

increasing from k_1 to k_2 with the maximum overlap, until $\delta_{\max}^p$ is reached, and an elastic branch with maximal stiffness k_2 is established (not shown in Fig. 1, see Ref. [SML15] for details). As a side-remark, the limit-slope k_2 can be introduced for practical reasons. If k_2 is not limited, the contact duration could become very small, i.e. the time step would have to be reduced below values that yield reasonable performance. However, there are also other – physical and mechanical – rea-

sons for an elastic cut-off [SML15]; how to avoid the elastic cut-off was presented in Ref. [SML15].

The linear interpolation in Eq. (7) is arbitrary: one can vary it depending on the material under consideration, using as additional parameter the power ψ, so that the stiffness

$$k_2^*(\delta_{\max}) = \begin{cases} k_2 & \text{if } \delta_{\max} \geq \delta_{\max}^p \\ k_1 + (k_2 - k_1)\left[\delta_{\max}/\delta_{\max}^*\right]^\psi & \text{if } \delta_{\max} < \delta_{\max}^p \end{cases} , \tag{8}$$

is non-linearly interpolated. This includes the linear case, for $\psi = 1$, as originally suggested [Lud08], the invariant stiffness, for $\psi = 0$, or the non-linear interpolation to provide Hertzian-type behavior of the coefficient of restitution, for $\psi = 1/2$, as first suggested in Ref. [SML15] (see Fig. 14), and more recently in Ref. [TCC17]. For different materials, different values of ψ might be more appropriate than those three cases, but the generalized Eq. (8) leaves this as an option to be chosen during parameter calibration.

While in the case of collisions of particles with large deformations, dissipation takes place due to the hysteretic nature of the force-law, stronger dissipation of small amplitude deformations is achieved by adding the viscous, velocity dependent dissipative force from Eq. (3) to the hysteretic force, such that $f^n = f^{\text{hys}} + \gamma_0 v_n$. The hysteretic model contains the linear contact model as the special case when $k_1 = k_2 = k$.

2.2.3 Long Range Normal Forces

Medium range van der Waals forces can be taken into account in addition to the hysteretic force such that $f^n = f^{\text{hys}} + f^{\text{vdW}}$ with, for example, the attractive part of a Lennard-Jones Potential

$$f^{\text{vdW}}(r_{ij}) = -6(\varepsilon/r_0)[(r_0/r_{ij})^7 - (r_0/r_c)^7] \quad \text{for } r_{ij} := |\vec{r}_i - \vec{r}_j| \leq r_c \,. \tag{9}$$

The new parameters necessary for this force are an energy scale ε, a typical length scale r_0 and a cut-off length r_c. As long as r_c is not much larger than the particle diameter, the methods for short range interactions can still be applied to such a medium range interaction model – only the linked cells have to be larger than twice the cut-off radius, since no force should be active for $r > r_c$. A piecewise linear non-contact force is proposed in Ref. [SML15] for both reversible and irreversible contact models that mimick van der Waals or Coulomb type interactions and liquid bridges that are hysteretic in nature, respectively.

2.3 Kinematics of Tangential Forces and Torques

For the tangential degrees of freedom, there are three different force- and torque-laws to be implemented: (i) friction, (ii) rolling resistance, and (iii) torsion resistance.

2.3.1 Sliding

For dynamic (sliding) and static *friction*, the relative tangential velocity of the contact points,

$$\vec{v}_t = \vec{v}_{ij} - \vec{n}(\vec{n} \cdot \vec{v}_{ij}) \ , \tag{10}$$

is to be considered for the force computations (or torque computations in subsection 2.4), with the total relative velocity of the particle surfaces at the contact

$$\vec{v}_{ij} = \vec{v}_i - \vec{v}_j + a_i' \vec{n} \times \vec{\omega}_i + a_j' \vec{n} \times \vec{\omega}_j \ , \tag{11}$$

with the corrected radius relative to the contact point $a_\alpha' = a_\alpha - \delta/2$, for $\alpha = i, j$. For strongly different particle sizes and large overlaps, this has to be considered in more detail [TWT]. Tangential forces and torques acting on the contacting particles are computed from the accumulated sliding and rolling/torsion of the contact points relative to each other, as described in detail in subsec. 2.4.1.

2.3.2 Objectivity

Objectivity is about the invariance of contact models in moving or rotating reference frames. In general, two particles can rotate together, due to either a global rotation of the reference frame or a non-central "collision". Either way, the angular velocity $\vec{\omega}_0 = \vec{\omega}_0^n + \vec{\omega}_0^t$, of the rotating reference has the tangential-plane component

$$\vec{\omega}_0^t = \frac{\vec{n} \times (\vec{v}_i - \vec{v}_j)}{a_i' + a_j'} \ , \tag{12}$$

which is related to the relative velocity, while the normal component, $\vec{\omega}_0^n$, is not. Inserting $\vec{\omega}_i = \vec{\omega}_j = \vec{\omega}_0^t$, from Eq. (12), into Eq. (11) leads to zero sliding velocity, proving that the above relations are objective. Tangential forces and torques due to sliding can become active only when the particles are rotating in the same direction with respect to the common rotating reference frame. For rolling and torsion, there is no similar relation between rotational and tangential degrees of freedom: for any rotating reference frame, torques due to rolling and torsion can become active only due to rotation of two particles relative to each other, in opposite direction, in the common reference frame.

Since action should be equal to reaction, the tangential forces are equally strong, but opposite, i.e., $\vec{f}_j^t = -\vec{f}_i^t$, while the corresponding torques are parallel but not necessarily equal in magnitude: $\vec{q}_i^{\,\text{friction}} = -a_i' \vec{n} \times \vec{f}_i$, and $\vec{q}_j^{\,\text{friction}} = (a_j'/a_i')\vec{q}_i^{\,\text{friction}}$. Note that tangential forces and torques *together* conserve the total angular momentum about the pair center of mass

$$\vec{L}_{ij} = \vec{L}_i + \vec{L}_j + m_i r_{i\text{cm}}^2 \vec{\omega}_0^t + m_j r_{j\text{cm}}^2 \vec{\omega}_0^t \ , \tag{13}$$

with the rotational contributions $\vec{L}_\alpha = I_\alpha \vec{\omega}_\alpha$, for $\alpha = i, j$, and the distances $r_{\alpha\text{cm}} = |\vec{r}_\alpha - r_\text{cm}|$ from the particle centers to the center of mass $\vec{r}_\text{cm} = (m_i \vec{r}_i + m_j \vec{r}_j)/(m_i +$

m_j), see Ref. [Lud98]. The change of angular momentum consists of the change of particle spins (first term) and of the change of the angular momentum of the two masses rotating about their common center of mass (second term):

$$\frac{d\vec{L}_{ij}}{dt} = \vec{q}_i^{\text{friction}} \left(1 + \frac{a'_j}{a'_i}\right) + \left(m_i r_{i\text{cm}}^2 + m_j r_{j\text{cm}}^2\right) \frac{d\vec{\omega}_0^t}{dt} \,, \tag{14}$$

which both contribute, but exactly cancel each other, since

$$\begin{aligned} \vec{q}_i^{\text{friction}} \left(1 + \frac{a'_j}{a'_i}\right) &= -(a'_i + a'_j)\, \vec{n} \times \vec{f}_i \\ &= -\left(m_i r_{i\text{cm}}^2 + m_j r_{j\text{cm}}^2\right) \frac{d\vec{\omega}_0^t}{dt} \,, \end{aligned} \tag{15}$$

see [Lud06] for more details.

2.3.3 Rolling

A *rolling* velocity $\vec{v}_r^0 = -a'_i\vec{n} \times \vec{\omega}_i + a'_j\vec{n} \times \vec{\omega}_j$, defined in analogy to the sliding velocity, is not objective in general [Els06, Lud06] – only in the special cases of (i) equal-sized particles or (ii) for a particle rolling on a fixed flat surface.

The rolling velocity should quantify the distance the two surfaces roll over each other (without sliding). Therefore, it is equal for both particles by definition. An *objective rolling velocity* is obtained by using the reduced radius, $a'_{ij} = a'_i a'_j/(a'_i + a'_j)$, so that

$$\vec{v}_r = -a'_{ij} \left(\vec{n} \times \vec{\omega}_i - \vec{n} \times \vec{\omega}_j\right) \,. \tag{16}$$

This definition is objective since any common rotation of the two particles vanishes due to the difference. A more detailed discussion of the issue of rolling is beyond the scope of this paper.

A rolling velocity will activate torques, acting against the rolling motion, e.g., when two particles are rotating anti-parallel with spins in the tangential plane. These torques are then equal in magnitude and opposite in direction, i.e., $\vec{q}_i^{\text{rolling}} = -\vec{q}_j^{\text{rolling}} = a_{ij}\, \vec{n} \times \vec{f}_r$, with the quasi-force $\vec{f}_r$, computed in analogy to the friction force, as function of the rolling velocity $\vec{v}_r$ in Eq. 16. The quasi-forces for both particles are opposite and equal but do not act on the centers of mass, so that the total momenta (translational and angular) are conserved.

2.3.4 Torsion

For *torsion resistance*, the relative spin along the normal direction

$$\vec{v}_o = a_{ij} \left(\vec{n} \cdot \vec{\omega}_i - \vec{n} \cdot \vec{\omega}_j\right) \vec{n} \,, \tag{17}$$

is to be considered, which activates torques when two particles are rotating anti-parallel with spins parallel to the normal direction. Torsion is not activated by a common rotation of the particles around the normal direction $\vec{n} \cdot \vec{\omega}_0 = \vec{n} \cdot (\vec{\omega}_i + \vec{\omega}_j)/2$, which makes the torsion resistance objective.

The torsion torques are equal in magnitude and directed in opposite directions, i.e., $\vec{q}_i^{\text{torsion}} = -\vec{q}_j^{\text{torsion}} = a_{ij}\,\vec{f}_o$, with the quasi-force $\vec{f}_o$, computed from the torsion velocity in Eq. 17, and also not changing the translational momentum. Like for rolling, the torsion torques conserve the total angular momentum.

2.3.5 Summary

The implementation of the tangential force computations for $\vec{f}_t$, $\vec{f}_r$, and $\vec{f}_o$ as based on $\vec{v}_t$, $\vec{v}_r$, and $\vec{v}_o$, respectively, is assumed to be identical, i.e., even the same subroutine is used, but with different parameters as specified below. The difference is that friction leads to a force in the tangential plane (changing both translational and angular momentum), while rolling- and torsion-resistance lead to quasi-forces in the tangential plane and the normal direction, respectively, changing the particles' angular momentum only. For more details on tangential contact models, friction, rolling and torsion, see Refs. [BUK+05, DvZTR05, Lud07, Lud06, Els06]. The contact laws are implemented in MercuryDPM [WTLB12b, TWLB12b, TWT].

2.4 Tangential Force and Torque Laws

The tangential contact model presented now is a single procedure (subroutine) that can be used to compute either sliding, rolling, or torsion resistance. The subroutine needs a relative velocity as input and returns the respective force or quasi-force as function of the accumulated deformation. The sliding/sticking friction model will be introduced in detail, while rolling and torsion resistance are discussed only where different.

2.4.1 Sliding/Sticking Friction Model

The tangential force is coupled to the normal force via Coulomb's law, i.e. an inequality: $f^t \leq f_C^s := \mu^s f^n$, see also Ref. [Rad]. For the sliding case one has dynamic friction as equality: $f^t = f_C^t := \mu^d f^n$. The dynamic and the static friction coefficients follow, in general, the relation $\mu^d \leq \mu^s$. The static situation requires an elastic spring in order to allow for a restoring force, i.e., a non-zero remaining tangential force in static equilibrium due to activated Coulomb friction.

If a purely repulsive contact is established, $f^n > 0$, and the tangential force is active. For an adhesive contact, Coulombs law has to be modified in so far that f^n is replaced by $f^n + k_c\delta$. In this model, the reference for a contact is no longer the zero force level, but it is the adhesive, attractive force level along $-k_c\delta$.

If a contact is active, one has to project (or better rotate) the tangential spring into the actual tangential plane, since the frame of reference of the contact may have rotated since the last time-step. The tangential spring

$$\vec{\xi} = \vec{\xi}' - \vec{n}(\vec{n} \cdot \vec{\xi}') \,, \tag{18}$$

is used for the actual computation, where $\vec{\xi}'$ is the old spring from the last iteration, with $|\vec{\xi}| = |\vec{\xi}'|$ enforced by appropriate scaling/rotation. If the spring is new, the tangential spring-length is zero, but its change is well defined after this first initiation step. In order to compute the changes of the tangential spring, a tangential test-force is first computed as the sum of the tangential spring force and a tangential viscous force (in analogy to the normal viscous force)

$$\vec{f}_0^t = -k_t \, \vec{\xi} - \gamma_t \vec{v}_t \,, \tag{19}$$

with the tangential spring stiffness k_t, the tangential dissipation parameter γ_t, and $\vec{v}_t$ from Eq. (10). As long as $|\vec{f}_0^t| \leq f_C^s$, with $f_C^s = \mu^s(f^n + k_c\delta)$, one has static friction and, on the other hand, for $|\vec{f}_0^t| > f_C^s$, sliding friction becomes active. As soon as $|\vec{f}_0^t|$ gets smaller than f_C^d, static friction becomes active again.

In the *static friction* case, below the Coulomb limit, the tangential spring is incremented

$$\vec{\xi}' = \vec{\xi} + \vec{v}_t \, \Delta t_{\mathrm{DEM}} \,, \tag{20}$$

to be used in the next iteration in Eq. (18), and the tangential force $\vec{f}^t = \vec{f}_0^t$ from Eq. (19) is used. In the *sliding friction* case, the tangential spring is adjusted to a length consistent with Coulombs condition, so that

$$\vec{\xi}' = -\frac{1}{k_t} \left(f_C^d \, \vec{t} + \gamma_t \vec{v}_t \right) \,, \tag{21}$$

with the tangential unit vector, $\vec{t} = \vec{f}_0^t / |\vec{f}_0^t|$, defined by Eq. (19), and thus the magnitude of the Coulomb force is used. Inserting $\vec{\xi}'$ from Eq. (21) into Eq. (19) during the next iteration will lead to $\vec{f}_0^t \approx f_C^d \vec{t}$. Note that $\vec{f}_0^t$ and $\vec{v}_t$ are not necessarily parallel in three dimensions. However, the mapping in Eq. (21) always works, rotating the new spring such that the direction of the frictional force is unchanged and, at the same time, limiting the spring in length according to Coulombs law. In short notation the tangential contact law reads

$$\vec{f}^t = f^t \vec{t} = \min \left(f_C, |\vec{f}_0^t| \right) \vec{t} \,, \tag{22}$$

where f_C follows the static/dynamic selection rules described above. The torque on a particle due to frictional forces at this contact is $\vec{q}^{\,\mathrm{friction}} = \vec{l}_i^c \times \vec{f}_i^c$, where $\vec{l}_i^c$ is the branch vector, connecting the center of the particle with the contact point. Note that the torque on the contact partner is generally different in magnitude, since $\vec{l}_i^c$ can be different, but is directed in the same direction; see subsection 2.3.2 for details.

The four parameters for the friction law are k_t, μ_s, $\phi_d = \mu_d/\mu_s$, and γ_t, accounting for tangential stiffness, the static friction coefficient, the dynamic friction ratio, and

the tangential viscosity, respectively. Note that the tangential force described above is identical to the classical Cundall-Strack spring only in the limits $\mu = \mu^s = \mu^d$, i.e., $\phi_d = 1$, and $\gamma_t = 0$. The sequence of computations and the definitions and mappings into the tangential direction can be used in 3D as well as in 2D.

2.4.2 Rolling Resistance Model

The four new parameters for rolling resistance are k_r, μ_r, ϕ_r and γ_r. The new parameters account for rolling stiffness, a static and dynamic rolling "friction" coefficient, and rolling viscosity, respectively. In the subroutine called, the rolling velocity $\vec{v}_r$ is used instead of $\vec{v}_t$ and the computed quasi-force $\vec{f}_r$ is used to compute the torques, $\vec{q}^{\text{rolling}}$, on the particles.

2.4.3 Torsion Resistance Model

The four new parameters for rolling resistance are k_o, μ_o, ϕ_0 and γ_o. The new parameters account for torsion stiffness, a static and dynamic torsion "friction" coefficient, and torsion viscosity, respectively. In the subroutine, the torsion velocity $\vec{v}_o$ is used instead of $\vec{v}_t$ and the projection is a projection along the normal unit-vector, not into the tangential plane as for the other two models. The computed quasi-force $\vec{f}_o$ is then used to compute the torques, $\vec{q}^{\text{torsion}}$, on the particles.

2.5 Background Friction

Note that the viscous dissipation takes place in a two-particle contact. In the bulk material, where many particles are in contact with each other, this dissipation mode is very inefficient for long-wavelength cooperative modes of motion [LCB$^+$94b, LCB$^+$94a]. Therefore, an additional damping with the background can be introduced, so that the total force on particle i is

$$\vec{f}_i = \sum_j \left(f^n \vec{n} + f^t \vec{t} \right) - \gamma_b \vec{v}_i \,, \tag{23}$$

and the total torque

$$\vec{q}_i = \sum_j \left(\vec{q}^{\text{friction}} + \vec{q}^{\text{rolling}} + \vec{q}^{\text{torsion}} \right) - \gamma_{br} a_i^2 \vec{\omega}_i \,, \tag{24}$$

with the damping artificially enhanced in the spirit of a rapid relaxation and equilibration. The sum in Eqs. (23) and (24) takes into account all contact partners j of particle i, but the background dissipation can be attributed to the medium between the particles. Note that the effect of γ_b and γ_{br} should be checked for each flow situation and new set of parameters: it should be small in order to exclude artificial over-damping.

The full set of parameters is summarized in table 1. Note that only a few parameters are specified with dimensions, while most parameters are expressed as dimensionless numbers.

Property	Symbol
Time unit	t_u
Length unit	x_u
Mass unit	m_u
Particle radius	a
Material density	ρ_p
Elastic stiffness (variable)	k_2
Maximal elastic stiffness	$k = k_2$
Plastic stiffness	k_1/k
Adhesion "stiffness"	k_c/k
Friction stiffness	k_t/k
Rolling stiffness	k_r/k
Torsion stiffness	k_o/k
Plasticity depth	ϕ_f
Coulomb friction coefficient	$\mu = \mu_d = \mu_s$
Dynamic to static friction ratio	$\phi_d = \mu_d/\mu_s$
Rolling "friction" coefficient	μ_r
Torsion "friction" coefficient	μ_o
Normal viscosity	$\gamma = \gamma_n$
Friction viscosity	γ_t/γ
Rolling viscosity	γ_r/γ
Torsion viscosity	γ_o/γ
Background viscosity	γ_b/γ
Background viscous torque	γ_{br}/γ

Table 1: Summary of the microscopic contact model parameters. The longer ranged forces and their parameters, ϵ, r_0, and r_c are not included here.

As computer algorithms work by definition with non-dimensional numbers, we also include into the table the mass, length, and time units used in the simulation. These can be the standard SI-units (1 kg, 1 m, and 1 s). However, mass, length and time are often scaled such that all other parameters are non-dimensional. For example, the units $m_u = (4/3)\pi\rho_p a^3$, $x_u = 2a$ and $t_u = \sqrt{2a/g}$ are used in section 6.

3 Hard-Particle Event-Driven Simulations

In this section, the hard-sphere Event-Driven (ED) model is introduced. Hard spheres can be considered as the limit of infinite stiffness or, equivalently, zero contact time t_c, of the previously presented soft spheres contact models. In many situations hard spheres are a good approximation of the real contact dynamics, even though details of the contact- or collision behavior of the particles are ignored. This is especially true when multi-particle contacts are irrelevant, as in highly agitated or low density states. Nevertheless, a generalized model is also introduced that takes into account the

finite contact duration of real particle collisions which, besides providing a physical parameter, considerably saves computing time, as it avoids the so called "inelastic collapse".

In the framework of the hard sphere model, particles are assumed to be perfectly rigid and follow an undisturbed motion until a collision occurs, as detailed below. Together with the fact that collisions occur instantaneously, it becomes possible to implement an event-driven simulation method [Lub91, LM98, ML04b, ML04a, Mil04]. ED simulations are usually orders of magnitude faster than their DEM soft particle equivalents. Nonetheless, it is important to remark that the ED algorithm was only recently implemented in parallel [Lub92, ML04b], a relevant aspect for today's overall computing efficiency; here we avoid to discuss this issue in detail, and only remark that, to our knowledge, event-driven parallel algorithms scale sub-optimal with the number of processors p, i.e. the speed-up reached was $p^{1/2}$ instead of p, the standard for DEM simulations.

The lack of physical information in the model allows a much simpler treatment of collisions than described in Section 2, by just using a collision matrix based on momentum conservation and energy loss rules. For the sake of simplicity, here we restrict ourselves to smooth hard spheres. Collision rules for rough spheres, that include friction coefficients, are extensively discussed elsewhere, see e.g. [LHMZ98, Lud09] and references therein.

3.1 Smooth Hard Sphere Collision Model

The standard interaction model for instantaneous collisions of identical particles with radius a, and mass m, is discussed in the following. The post-collisional velocities $\vec{v}'$ of two collision partners in their center of mass reference frame are given, in terms of the pre-collisional velocities $\vec{v}$, by

$$\vec{v}'_{1,2} = \vec{v}_{1,2} \mp (1+r)\vec{v}_n \,/2 \,, \tag{25}$$

with $\vec{v}_n \equiv [(\vec{v}_1 - \vec{v}_2)\cdot\vec{n}]\,\vec{n}$, the normal component of the relative velocity $\vec{v}_1 - \vec{v}_2$, parallel to $\vec{n}$, the unit vector pointing along the line connecting the centers of the colliding particles. The restitution coefficient $r \in [0,1]$ is a measure of the level of inelasticity in every collision, with $r = 1$ corresponding to the elastic case. If two particles collide, their velocities are changed according to Eq. (25), with the corresponding change of the translational energy at a collision

$$\Delta E = -m_{12}(1-r^2)v_n^2/2 \,, \tag{26}$$

with the reduced mass $m_{12} = m_1 m_2/(m_1+m_2)$.

3.2 Event-Driven Algorithm

The fundamental difference between an event-driven (ED) algorithm and a DEM soft-particle simulation lies in the handling of the time evolution. ED simulations do not possess a fixed time step, as DEM simulations, but a variable one, given always by the immediately next event. An event is either the collision of two particles, or the collision of one particle with a boundary, either physical or virtual. In the following, the conditions needed to use this approach are detailed, as also several optimization techniques for the definition of the next event.

The algorithm essentially consists of a cycle where the minimum of all future collision times is determined, and then the proper collision rule is selected and executed. ED simulations are thus extremely efficient when the time of the upcoming events can be analytically computed. This is the case for a constant and homogeneous external field (usually gravity) and infinitely hard spheres, as the solution for the time of collision between two particles is actually given just by the intersection of their relative linear trajectories. Walls, on the other hand, involve the solution of a quadratic equation. Nevertheless, let us remark that although analytic determination of the collision times highly simplifies the algorithm, the possibility of numerically solving the intersections of the equations of motion is also possible, and has been recently successfully implemented [BSL11].

The critical optimization point for serial ED algorithms is in the determination of the forthcoming collision times. The introduction of cells with virtual boundaries greatly increases the efficiency of this process. Virtual boundaries collisions have no effect on the particles motion, but are only introduced to keep track of which particles belong to which cell. If all the particles with centers in a given cell and its neighboring cells are known, then the search for possible collision partners for a particle in the cell can be done locally. That is, instead of having to check all pairs of particles for possible collisions, only local neighbors are considered, greatly reducing the time for the determination of the next collision.

Another source of optimization involves the treatment of collisions. Simple ED algorithms update the whole system after each event, a method which is straightforward but inefficient for large numbers of particles. In Ref. [Lub91] an ED algorithm was introduced which updates only those two particles involved in the last collision. The fact that the algorithm is "asynchronous", in so far that an event, i.e. the *next* event, can occur anywhere in the system, makes parallelization a big challenge [ML04b]. For the serial algorithm, a double buffering data structure is implemented, which contains the 'old' status and the 'new' status, each consisting of: time of event, positions, velocities, and event partners. When a collision occurs, the 'old' and 'new' status of the participating particles are exchanged. Thus, the former 'new' status becomes the actual 'old' one, while the former 'old' status becomes the 'new' one and is then free for the calculation and storage of possible future events. This seemingly complicated exchange of information is carried out extremely simply and fast by only exchanging the pointers to the 'new' and 'old' status respectively. Note that the 'old' status of

particle i has to be kept in memory, in order to update the time of the next contact, t_{ij}, of particle i with any other object j if the latter, independently, changed its status due to a collision with yet another particle. During the simulation such updates may be necessary several times so that the predicted 'new' status has to be modified.

The minimum of all t_{ij} is stored in the 'new' status of particle i, together with the corresponding partner j. Depending on the implementation, positions and velocities after the collision can also be calculated. This would be a waste of computer time, since before the time t_{ij}, the predicted partners i and j might be involved in several collisions with other particles, so that we apply a delayed update scheme [Lub91]. The minimum times of event, i.e. the times which indicate the next event for a certain particle, are stored in an ordered heap tree, such that the next event is found at the top of the heap with a computational effort of $O(1)$; changing the position of one particle in the tree from the top to a new position needs $O(\log N)$ operations. The search for possible collision partners is accelerated by the use of a standard linked-cell data structure and consumes $O(1)$ of numerical resources per particle. In total, this results in a numerical effort of $O(N \log N)$ for N particles. For a detailed description of the algorithm see Ref. [Lub91].

Using all these optimizations, we are able to simulate about 10^6 particles within reasonable time on a low-end PC [LH99], where the particle number is more limited by memory than by CPU power. Parallelization, however, is a means to overcome the limits of one processor [ML04b]. Since we could be interested in the behavior of granular particles possibly evolving over several decades in time, the fastness of the event-driven method becomes a crucial feature even for systems with low number of particles.

As a final remark concerning ED, one should note that the disadvantages connected to the assumptions made that allow to use an event driven algorithm limit the applicability of this method. Within their range of applicability, ED simulations are typically much faster than DEM simulations, since the former accounts for a collision in one basic operation (collision matrix), whereas the latter requires order of 40 basic steps (integration time steps). Note that this statement is also true in the dense regime. In the dilute regime, both methods give equivalent results, because collisions are mostly binary [LCB$^+$94a]. When the system becomes denser, multi-particle collisions can occur and the rigidity assumption within the ED hard sphere approach becomes invalid. For a recent study on soft, hard and rigid particles at moderate to high densities above the fluid-solid transition, see Ref. [VL16] and references therein, where it is shown that rigid particles have a strictly limit in density where the confining stress diverges, whereas soft particle systems can be compressed further given the confining stress is large enough. For the densities that can be reached using hard spheres, see Ref. [OL13], where it is shown that the limit density can be approached up to the numerical accuracy, and how this limit density depends on the polydispersity of the particles (their size distribution and its moments).

While softness can not be easily introduced into an ED algorithm, another effect can be elegantly considered: The most striking difference between hard and soft spheres

is the fact that soft particles dissipate less energy when they are in contact with many others of their kind. With other words, dissipation takes a finite time during, t_c, the Time of Contact (TC), which decreases with increasing stiffness of the particles. So while ED still builds upon binary collisions, at very high densities, permanent multiple contacts are taken mimicked by multiple collisions within the contact duration t_c. In the following chapter, the so called TC model is discussed as a means to account for the stiffness dependent contact duration in the hard sphere model.

4 Linking ED and DEM via the TC Model

In the hard-sphere ED method the contact duration is implicitly zero, matching well the corresponding assumption of instantaneous contacts used in kinetic theory [Haf83, JR85]. Due to this artificial simplification (which disregards the fact that a real contact takes always finite time) ED algorithms run into problems when the time between events $t_{\rm n}$ gets too small: in very dense systems with strong dissipation, $t_{\rm n}$ may even tend towards zero, which leads to a diverging dissipation rate; see Eq. (26). As a consequence the so-called "inelastic collapse" can occur, i.e. the divergence of the number of events per unit time. The problem of the inelastic collapse [MY94] can be avoided using restitution coefficients dependent on the time elapsed since the last event [LM98, LG03]. For the contact that occurs at time t_{ij} between particles i and j, one uses $r = 1$ if at least one of the partners involved had a collision with another particle later than $t_{ij} - t_{\rm c}^e$. The time $t_{\rm c}^e$ can be seen as a typical Time of Contat (TC), or contact duration, and allows for the definition of the dimensionless ratio

$$\tau_c = t_c^e/t_n \ . \tag{27}$$

The effect of $t_{\rm c}^e$ on the simulation results is negligible for large r and small $t_{\rm c}^e$; for a more detailed discussion see [LM98, LH99, LG03].

In assemblies of soft particles, multi-particle contacts are possible and the inelastic collapse is naturally avoided, since the dissipation rate is always finite (less than $\Delta E/t_c^e$). The TC model can be seen as a means to approximate multi-particle collisions for hard spheres in dense systems [LCRD96, Lud97, LM98]. Let us consider the homogeneous cooling system (HCS) to evaluate the influence of the TC model in the cooling dynamics. One can explicitly compute the corrected cooling rate (r.h.s.) in the energy balance equation

$$\frac{d}{d\tau}E = -2I(E, t_c^e) \ , \tag{28}$$

with the dimensionless time $\tau = (2/3)At/t_E(0)$ for 3D systems, scaled by $A = (1-r^2)/4$, and the collision rate $t_E^{-1} = (12/a)\nu g(\nu)\sqrt{T/(\pi m)}$, with $T = 2K/(3N)$. In these units, the energy dissipation rate I is a function of the dimensionless energy $E = K/K(0)$ and the cut-off time t_c^e, with K the kinetic energy. In this representation, the restitution coefficient is hidden in the rescaled time via $A = A(r)$,

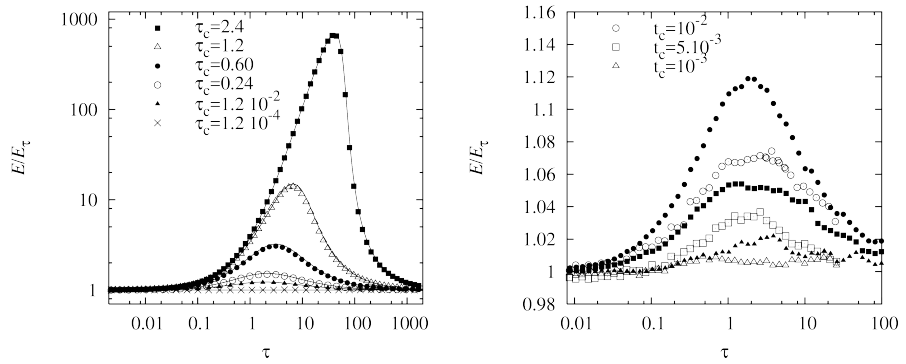

Figure 2: (Left) Deviation from the HCS, i.e. rescaled energy E/E_τ, where E_τ is the classical solution $E_\tau = (1+\tau)^{-2}$. The data are plotted against τ for simulations with different $\tau_c(0) = t_c^e/t_E(0)$ as given in the key/inset, with $r = 0.99$, and $N = 8000$. Symbols are ED simulation results, the solid line results from the third order correction. (Right) E/E_τ plotted against τ for simulations with $r = 0.99$, and $N = 2197$. Solid symbols are ED simulations, open symbols are DEM (soft particle simulations) with three different t_c^e as given in the inset.

so that inelastic hard sphere simulations with different r scale on the same master-curve. When the classical dissipation rate $E^{3/2}$ [Haf83] is extracted from I, so that $I(E, t_c^e) = J(E, t_c^e)E^{3/2}$, one has the correction-function $J \to 1$ for $t_c \to 0$. The deviation from the classical HCS is [LG03]:

$$J(E, t_c^e) = \exp\left(\Psi(x)\right) \ , \tag{29}$$

with the series expansion $\Psi(x) = -1.268x + 0.01682x^2 - 0.0005783x^3 + \mathcal{O}(x^4)$ in the collision integral, with $x = \sqrt{\pi} t_c^e t_E^{-1}(0)\sqrt{E} = \sqrt{\pi}\tau_c(0)\sqrt{E} = \sqrt{\pi}\tau_c$ [LG03]. This is close to the result $\Psi_{\rm LM} = -2x/\sqrt{\pi}$, proposed by Luding and McNamara, based on probabilistic mean-field arguments [LM98], where $\Psi_{\rm LM}$ thus neglects non-linear terms and underestimates the linear part.

Given the differential equation (28) and the correction due to multi-particle contacts from Eq. (29), it is possible to obtain the solution numerically, and to compare it to the classical $E_\tau = (1+\tau)^{-2}$ solution. Simulation results are compared to the theoretical solution in Fig. 2 (left). The agreement between simulations and theory is almost perfect in the examined range of t_c^e values; only when deviations from homogeneity are evidenced one expects disagreement between simulation and theory. The fixed cut-off time t_c^e has no effect when the time between collisions is very large $t_E \gg t_c^e$, but strongly reduces dissipation when the collisions occur with high frequency $t_E^{-1} \gtrsim (t_c^e)^{-1}$. Thus, in the homogeneous cooling state, there is a strong effect initially when t_c is large, but the long time behavior tends towards the classical decay $E \to E_\tau \propto \tau^{-2}$.

The next verification of the ED results obtained using the TC model involves comparing them to DEM simulations, see Fig. 2 (right). Open and solid symbols correspond to soft and hard sphere simulations, respectively, where the qualitative behavior (the deviation from the classical HCS solution) is identical. The energy decay is delayed due to multi-particle collisions, but later the classical solution is recovered. A quantitative comparison shows that the deviation of E from E_τ is larger for ED than for DEM, given that the same t_c^e is used. This weaker dissipation can be understood from the strict rule used for ED: dissipation is inactive if any particle had a contact already. The disagreement between ED and DEM is systematic and should disappear if an about 30 per-cent smaller t_c value is used for ED. The disagreement is also plausible, since the TC model disregards all dissipation for multi-particle contacts, while the soft particles still dissipate energy — even though much less — in the case of multi-particle contacts.

The above results show that the TC model is in fact a good method to approximate soft particles behaviour with hard particles. The only modification made to straightforward ED involves a reduced dissipation for (rapid) multi-particle collisions. More general corrections and adaptations are the subject of ongoing work.

5 Micro-macro Transition for Particle Simulations

To analyse the static or dynamic behaviour of granular assemblies, bulk properties such as the continuum (macro) fields of mass density ρ, velocity $\vec{V}$, velocity gradient $\nabla\vec{V}$ and stress $\underline{\underline{\sigma}}$ can be extracted from the discrete (micro) particle data. These fields are related to each other via the equations of mass and momentum conservation,

$$\frac{\partial \rho}{\partial t} + \nabla \cdot (\rho \vec{V}) = 0, \tag{30a}$$

$$\frac{\partial (\rho \vec{V})}{\partial t} + \nabla \cdot (\rho \vec{V} \otimes \vec{V}) = -\nabla \cdot \underline{\underline{\sigma}} + \rho \vec{g} + \vec{t}, \tag{30b}$$

and thus the definitions of these fields should satisfy above equations. Here, we use the compressive stress definition such that the pressure, $p = \mathrm{tr}(\underline{\underline{\sigma}})/3$, is positive under compression. The body force density, $\rho\vec{g}$, accounts in this case for gravity, while the external interaction force density, $\vec{t}$, accounts for interactions of the bulk with external objects, such as boundaries [WTLB12b] or drag relations with other constituents in a mixed flow [WLT13].

While it is relatively straightforward to define these fields for homogeneous mixtures, defining locally and temporally varying fields requires some care. Here, we present the coarse-graining formulation [Bab97, Gol10, WTLB12b], where the field definitions are constructed directly from equations (30) and thus satisfy them exactly.

First, the macroscopic density is defined by

$$\rho(\vec{r},t) = \sum_{i=1}^{N} m_i \mathcal{W}\left(\vec{r} - \vec{r}_i(t)\right), \tag{31}$$

where we have replaced the Dirac delta function of the micromechanical density definition, $\rho^{\text{mic}} = \sum_{i=1}^{N} m_i \delta\left(\vec{r} - \vec{r}_i\right)$, by an integrable 'coarse-graining' function $\mathcal{W}$ whose integral over the domain is unity and has a predetermined (non-dimensional) width (or coarse-graining scale) $w = w'/d$, with the dimensional width w', relative to the particle diameter. The resolution and shape of the coarse-graining function used in the formulation can be chosen freely, such that both microscopic and macroscopic effects can be studied. Many shape functions are possible, such as Gaussian distributions or Lucy functions. While the shape of the coarse-graining function has little effect on the macroscopic fields, they depend on the coarse-graining width, see [WLT13] and section 6.3.

Next, the coarse-grained (CG) macroscopic momentum density is defined by

$$\vec{p}(\vec{r},t) = \sum_{i=1}^{N} m_i \vec{v}_i \mathcal{W}(\vec{r} - \vec{r}_i), \tag{32}$$

so that the macroscopic velocity field is defined as the ratio of momentum and density fields,

$$\vec{V}(\vec{r},t) = \vec{p}(\vec{r},t)/\rho(\vec{r},t). \tag{33}$$

Substituting (31) and (33) into (30a) and simplifying shows that the continuity equation is indeed satisfied, as shown in [Gol10, Bab97].

Finally, we consider the momentum conservation equation with the aim of establishing the macroscopic stress field, $\underline{\underline{\sigma}}$. We split the stress

$$\underline{\underline{\sigma}} = \underline{\underline{\sigma}}^k + \underline{\underline{\sigma}}^c, \tag{34a}$$

into its kinetic and contact contributions,

$$\underline{\underline{\sigma}}^k = \sum_{i=1}^{N} m_i \vec{v}_i' \otimes \vec{v}_i' \mathcal{W}(\vec{r} - \vec{r}_i), \tag{34b}$$

$$\underline{\underline{\sigma}}^c = -\sum_{i=1}^{N} \sum_{j=1}^{N+N_w} \vec{f}_{ij} \otimes \vec{l}_{ij} \int_0^1 \mathcal{W}(\vec{r} - \vec{r}_i + s\vec{l}_{ij})\, \mathrm{d}s, \tag{34c}$$

with interaction forces $\vec{f}_{ij} = -\vec{f}_{ji}$ and center-contact vectors $\vec{l}_{ij} = \vec{r}_i - \vec{c}_{ij}$, where $\vec{c}_{ij}$ denotes the contact point between the particle i and particle/wall j and where the indices $N+1$ to $N+N_w$ denote contacts with external objects. Further, the fluctuation velocity of particle i is defined by

$$\vec{v}_i'(\vec{r},t) = \vec{v}_i(t) - \vec{V}(\vec{r},t), \tag{35}$$

and the external interaction force density (IFD) is defined as

$$\vec{t} = \sum_{i=1}^{N} \sum_{k=N+1}^{N+N_e} \vec{f}_{ij} \mathcal{W}(\vec{r} - \vec{c}_{ij}). \tag{36}$$

Substituting (34-36) into (30b) shows that momentum conservation is exactly satisfied. Thus, the results are valid even for single particles and at one moment in time, as no ensemble averaging is required to satisfy the mass and momentum balance. This was first shown in [Gol10] without considering body forces and external forces, and in [WTLB12b] for the full system. One can continue to define other fields in this fashion, such as heat flux and internal energy from the energy equation [Bab97], and the couple stress from the conservation of local angular momentum [Gol10].

The definition of the stress tensor (34c) was shown to be unique under additional symmetry requirements [WAD95]. Note that one can perform the integration in (34c) analytically and obtain an explicit expression, hence the computational cost of this formula is not more expensive than other expressions. Further note that the integral of (34) over the whole volume V satisfies the virial definition of mechanical stress in a volume V,

$$\underline{\underline{\sigma}} = \frac{1}{V} \left(\sum_{i=1}^{N} m_i \vec{v}_i' \otimes \vec{v}_i' - \sum_{i=1}^{N} \sum_{j=1}^{N+N_w} \vec{f}_{ij} \otimes \vec{l}_{ij} \right). \tag{37}$$

Averaging over a time interval Δt and replacing the temporal average over the force vector $\vec{f}_{ij}$ by the change of momentum $\Delta \vec{p}_{ij}$ for each collision of particle i with particle/wall j in the time interval Δt, one obtains for hard spheres [LM98, Lud98]

$$\bar{\underline{\underline{\sigma}}} = \frac{1}{V \Delta t} \left(\int_t^{t+\Delta t} \sum_{i=1}^{N} m_i \vec{v}_i' \otimes \vec{v}_i' \, \mathrm{d}t - \sum_{i=1}^{N} \sum_{j=1}^{N+N_e} \Delta \vec{p}_{ij} \otimes \vec{l}_{ij} \right), \tag{38}$$

which connects the soft DEM models with the rigid ED models also on the macroscopic level.

6 Granular chute flow

Granular chute flows are investigated as first exemplary case, in the steady, continuous inertial flow regime. The system, its flow-states and a closure for a shallow-layer continuum model were described in more detail in [WTLB12a, WHTL13, TWLB12a, TWOL13].

The following is a brief review of the more detailed results presented in [WHTL13]. Here, we describe the system setup and parameters in subsections 6.1 and 6.2. In subsection 6.3, we investigate the sensitivity of the macroscopic fields on the width w. Finally we discuss the resulting rheology in subsections 6.4 and 6.5.

6.1 Model system

A Cartesian coordinate system is used where x denotes the flow direction, y the in-plane vorticity direction, and z the height direction normal to the base. The parameters of the system are non-dimensionalized such that the particles' diameter is $\tilde{d} = 1$, their mass is $\tilde{m} = 1$, and the magnitude of gravity is $\tilde{g} = 1$, so that the unit of time becomes $t_u = \sqrt{d/g}$. For the sake of simplicity, the tilde indicating dimensionless quantities is now dropped. The chute is inclined at an angle θ such that gravity acts in the direction $\vec{g} = (\sin\theta, 0, -\cos\theta)^T$. The simulation cell has dimensions 20×10 in the x- and y-directions and is periodic in these directions. The base of the system is a rough surface consisting of N_e fixed particles, see Figure 3 and Ref. [WTLB12a] for details. N monodispersed flowing particles are introduced to the system at random non-overlapping positions well above the base. Due to gravity they fall and accelerate down the slope until they reach a steady state (before $t = 2000$). Macroscopic fields are then extracted and analysed from the steady state data from $t = 2000$ to $t = 2500$.

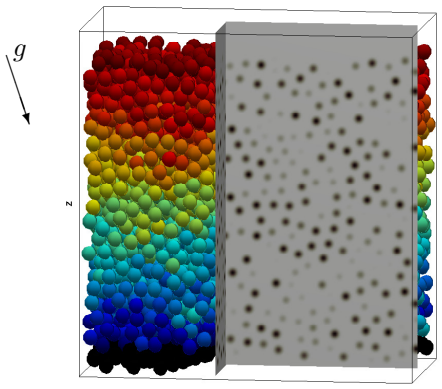

Figure 3: Snapshot of steady-state inertial granular chute flow of $N = 6000$ flowing particles over a rough surface inclined at $\theta = 28°$, with colour indicating speed. The vertical slices show the density $\rho(t, x, y, z)$ using a Lucy function of width $w = 1/2$.

6.2 Material and system parameters

We use a linear viscoelastic normal force model with sliding friction in tangential direction. The dimensionless normal spring and damping constants are $\tilde{k} = 2 \cdot 10^5$ and $\tilde{\gamma} = 50$, respectively; thus, the contact duration for pair collisions is $\tilde{t}_c = 0.005$ and the coefficient of restitution is $r = 0.88$. The tangential spring and damping constants are $k^t/k = 2/7$ and $\gamma^t = \gamma$, such that the frequency of normal and tangential contact oscillation are similar, and the normal and tangential dissipation are comparable. The

microscopic friction coefficient is set to $\mu_d = \mu_s = 0.5$. Contacts between two flowing particles and between flowing and fixed base particles are treated equally. The system is integrated using the Velocity-Verlet algorithm with a time step of $dt = t_c/50$. The simulations are implemented in MercuryDPM [TKdV$^+$13, TKF$^+$13, TWT].

6.3 Scale dependence of the macroscopic fields

Depth profiles for steady uniform flow are obtained using a Lucy coarse-graining function of width w, and averaging over $x \in [0, 20]$, $y \in [0, 10]$, and $t \in [2000, 2500]$. The spatial averaging is done analytically, while we average in time with snapshots taken every $t_c/2$.

The macroscopic fields can vary strongly with w, which therefore has to be carefully selected. According to Goldenberg *et al.* [GAC$^+$06], each well-defined macroscopic field should yield a plateau for a range of w-values, where the field (ideally) does not depend on the coarse-graining scale w. For smaller w-values, statistical fluctuations are strong and longer time-averaging or ensemble-averaging is required to obtain useful data. For larger w, the coarse-graining is expected to cause an unphysical smoothing of the field gradients.

Figure 4 shows the volume fraction profile, $\nu(z) = \rho(z)/\rho_p$, for different w. A plateau, as described above, exists for all heights in the range $0.0025 \leq w \leq 0.1$. On this length scale, the volume fraction is nearly independent of z, while oscillations due to layering of the flow can be observed when approaching the base boundary. All other macroscopic fields show a similar plateau.

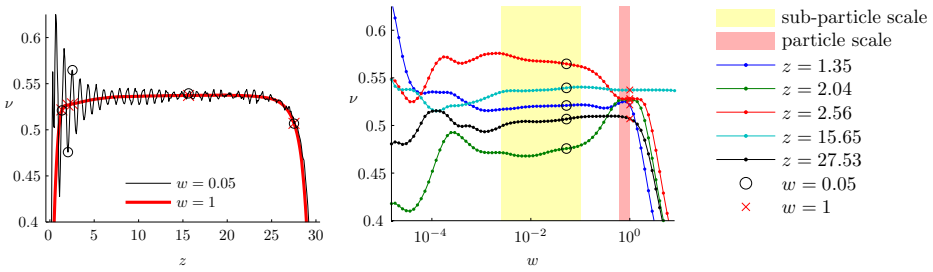

Figure 4: (Left) Density as a function of height, for $w = 0.05$ and $w = 1$. (Right) Density at selected heights as a function of the coarse-graining width w. Circles and crosses in both figures denote the density at the selected heights for $w = 0.05$ and $w = 1$, respectively. Data is taken for $N = 6000$, $\theta = 28°$, as in Ref. [WHTL13].

Further, a second, wider plateau can be observed for $0.6 \leq w \leq 1$ in the bulk of the flow, further than $2w$ away from the wall. On this scale, the oscillations due to layering are unresolved, which leads to smooth density, velocity and contact stress

fields. Only the kinetic stress is scale-dependent, as first shown in [GG01]; however, this scale-dependence can be quantified and removed [WHTL13].

6.4 Stress and boundary conditions

Assuming that the flow is steady and uniform, Eq. (30b) reduces to

$$\frac{\partial}{\partial z}\sigma_{\alpha z} = -\rho g_\alpha - t_\alpha, \quad \alpha = x, y, z, \tag{39}$$

which is in excellent agreement with the stress and external force density profiles [58].

Eq. (39) is called the lithostatic stress relation, since it determines (three) stress components in terms of the density ρ. Since the external interaction force density, $\vec{t}$, is zero everywhere except within an coarse-graining length distance from the basal surface, the slope of $\sigma_{\alpha z}$ equals $-\rho g_\alpha$ everywhere except near the base boundary. Due to the momentum balance (39), both the bulk friction, $\mu = -\sigma_{xz}/\sigma_{zz}$, and the friction due to the interactions with the base, $-t_x/t_z$, are equal to $\tan\theta$ and thus constant for all heights. Further, in all simulations, the stress tensor was found to be nearly symmetric, with the asymmetric part contributing less than 0.1% to the deviatoric stress components.

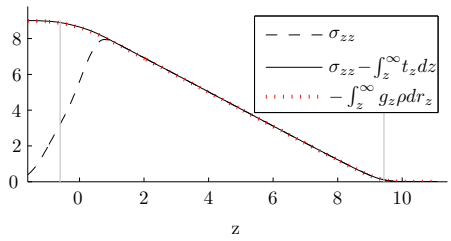

Figure 5: Downward normal stress, see inset, without (dashed) and with (solid) correction by the external IFD for $w = 1/4$. The extended stress, $\sigma'_{zz} = \sigma_{zz} - \int_z^\infty t_z\, dz$, defined in (40) exactly matches the weight of the flow above height z (red dotted line), as expected for steady flows. Grey vertical lines indicate bed and surface location, calculated using the points where the extended stress definition vanishes and reaches its maximum value (to within 2%), as in Ref. [WTLB12a].

Since the external interaction force density, $\vec{t}$, is zero everywhere except close to the basal surface, the gradients of $\vec{t}$ and $\underline{\underline{\sigma}}$ are very steep at the base. Thus, $\vec{t}$ should be incorporated into the continuum equation as a boundary condition rather than a continuous field [WHTL13]. To accomplish this, we introduce the *extended stress*,

$$\sigma^{\text{ext}}_{\alpha z} = \sigma_{\alpha z} + \int_z^\infty t_{\alpha z} \mathrm{d}z\ , \tag{40}$$

which yields the boundary condition,

$$\lim_{z\to-\infty}\sigma^{\mathrm{ext}}_{\alpha z}=\int_{-\infty}^{\infty}t_{\alpha z}\mathrm{d}z\,. \tag{41}$$

Substituting (39) into (40) thus yields a simple relation between stress and density,

$$\sigma^{\mathrm{ext}}_{\alpha z}=\int_{z}^{\infty}\rho g_\alpha\mathrm{d}z,\quad \lim_{z\to-\infty}\sigma^{\mathrm{ext}}_{\alpha z}=\int_{-\infty}^{\infty}\rho g_\alpha\mathrm{d}z=Nmg_\alpha, \tag{42}$$

which produces a smooth extended stress field, as shown in Figure 5.

6.5 Inertial number

A widely accepted basic rheological model for granular flows – in the dense, quasi-static and inertial regimes – is the so-called $\mu(I)$-rheology [dCEP$^+$05, IK04, MiD04, JFP06]. Many experimental and numerical studies suggest that the mass density ρ and the macroscopic (bulk) friction μ are functions of the inertial number,

$$I=\dot\gamma d\sqrt{\rho_p/p}, \tag{43}$$

where $\dot\gamma=\frac{\partial V_x}{\partial z}$ is the shear rate, d the particle diameter, p the (compressive) pressure and ρ_p the particle density, which is assumed constant for all heights.

Deriving the shear rate profile from the velocity field, we plot the inertial number as a function of height in Figure 6. It shows that the inertial number is indeed constant in the bulk, but varies significantly near both base and surface. Thus, we define the bulk of the flow to be the region where I is within 10% of the median value.

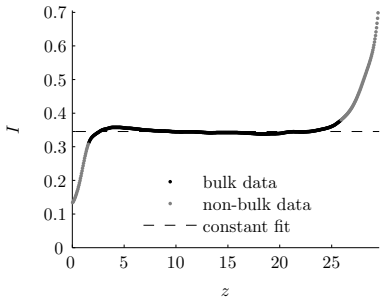

Figure 6: Inertial number plotted as a function of height, for $w=1$, $\theta=28^\circ$ and $N=6000$, The dashed line shows the constant inertial number as predicted by the $\mu(I)$ rheology.

6.6 An objective description of the stress tensor

Next, we generalise the $\mu(I)$ rheology from a Cartesian frame to a rheological model for general flow situations by using (objective) invariants of the tensors, and quantify all non-Newtonian mechanisms that the chute flow features.

For a symmetric stress, when the σ_{xy}, σ_{yz} components are close to zero in steady state, the orientation of the deviatoric stress tensor is determined solely by measuring the orientation ϕ_σ of the largest principal stress in the xz-plane. Then the stress takes the form [WHTL13, HGWL12]

$$\underline{\underline{\sigma}} = p\underline{\underline{I}} + \underline{\underline{R}} \cdot \begin{pmatrix} \lambda_1 & 0 & 0 \\ 0 & \lambda_2 & 0 \\ 0 & 0 & \lambda_3 \end{pmatrix} \cdot \underline{\underline{R}}^T, \tag{44}$$

with the transformation matrix

$$\underline{\underline{R}} = \begin{pmatrix} \cos\phi_\sigma & 0 & \sin\phi_\sigma \\ 0 & 1 & 0 \\ -\sin\phi_\sigma & 0 & \cos\phi_\sigma \end{pmatrix} \tag{45}$$

where the second term is the deviatoric stress, with $\lambda_1 + \lambda_2 + \lambda_3 = 0$. To quantify the anisotropy of the stress tensor, we further decompose the deviatoric stress into: (*i.*) the "anisotropy" of the deviatoric stress, i.e. the ratio of deviatoric stress (norm) and pressure,

$$s_D^\star := \frac{1}{\sqrt{6}p}\sqrt{(\lambda_1-\lambda_2)^2 + (\lambda_2-\lambda_3)^2 + (\lambda_3-\lambda_1)^2}\,, \tag{46a}$$

see Ref. [TML]. (*ii.*) the anisotropic stress distribution between the principal directions,

$$\Lambda_{12} := -\lambda_2/\lambda_1, \tag{46b}$$

and (*iii.*) the orientation of its eigensystem,

$$\Delta\phi := \phi_\sigma - \phi_\epsilon, \tag{46c}$$

where $\phi_\epsilon = 45^\circ$ denotes the orientation angle of the strain rate tensor.

Thus, three objective variables are obtained that fully describe the deviatoric stress tensor and thus determine the flow behaviour. For isotropic flows, we recover the original $\mu(I)$ rheology where $\Delta\phi_\sigma = 0$, $\Lambda_{12} = 0$, $\sigma_{zz}/p = 1$ and $s_D^\star = \mu(I)$.

Simulation results show that the flow rheology is indeed well-described by the inertial number, as shown in figure 7. The anisotropy $s_D^\star$, follows a similar curve as the Cartesian bulk friction μ and is therefore fitted by the curve described in [MiD04]. However, the results show clearly, that non of the Newtonian flow assumptions is satisfied. Λ_{12} deviates from their respective Newtonian values even for small inertial numbers, while $\Delta\phi_\sigma$ deviates from zero with increasing inertial number. Remarkably, the simple $\mu(I)$-rheology represents the dominant mechanism, while the others are relatively small. A generalization for other flow situations is in progress [KLM14, KIML13].

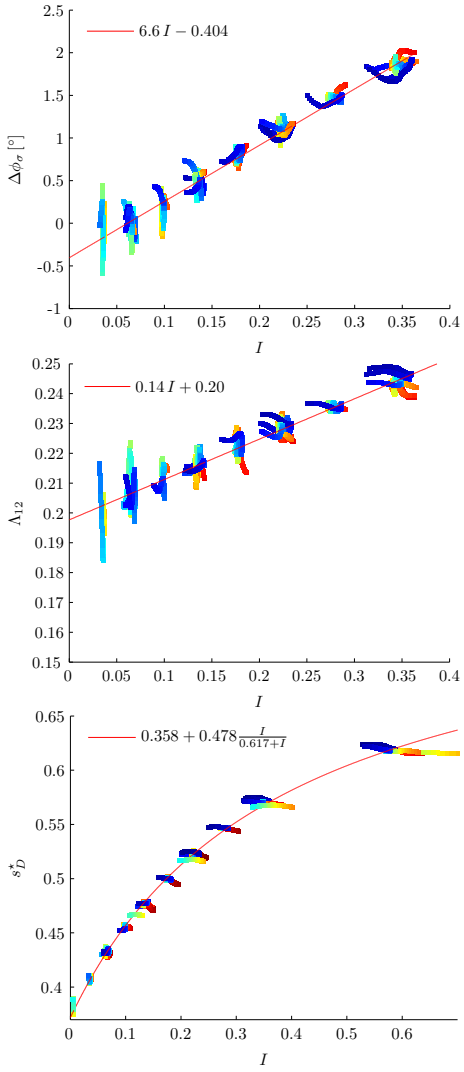

Figure 7: Three objective variables that describe the deviatoric stress tensor, are plotted against the inertial number I. Shade/color indicates relative height z from bottom (blue) to top (red). Lines indicate fits to the bulk data as specified in the insets/keys. *Top:* Angular deviation of the deviatoric stress from collinearity with the strain rate tensor, $\Delta\phi_\sigma$, with linear fit. *Middle:* Ratio of eigenvalues Λ_{12} with linear fit. *Bottom:* Magnitude of the deviatoric stress ratio, $s^\star_D$, with the line a fit to the bulk data. Data are bulk values from steady simulations in the parameter range $4000 \leq N \leq 8000$, $20^\circ \leq \theta \leq 28^\circ$, with coarse graining width $w = 1$, using the reduced kinetic stress [WHTL13].

6.7 Summary

In summary, the micro-macro transition has been successfully applied to steady, inertial granular flows down an inclined plane. The fields are well defined (almost independent of w) if the coarse-graining length-scale w is chosen carefully, either on the particle scale $w \sim 1$ or on the sub-particle resolution scale $w \sim 0.05$. We discussed the macroscopic fields and showed how to interpret the external interaction force density $\vec{t}$ as a boundary condition. The simulation results were then analysed to obtain an objective and complete tensorial rheological model for steady, planar non-Newtonian granular flows, involving all further non-Newtonian mechanisms (as possible in this situation) on top of the classical $\mu(I)$-rheology.

7 Vibrated granular bed

Our second example consists of a vertically vibrated bed of grains. In this case we take the limit of hard-spheres and compare the macroscopic states obtained by ED simulations with both previous experimental realizations and DEM simulations. We compute the macroscopic fields of packing fraction, pressure and temperature from both ED and DEM simulations using different coarse-graining methods. We then study their agreement as a function of the DEM collision time parameter t_c. Even though the system presents highly packed regions, it is expected that the hard particle approximation does not have a big influence on the observed dynamics, as the system is constantly fluidized, thus minimizing the influence of multi-particle contacts. Indeed, a very good agreement between simulations and experiments is found, as also between the macroscopic fields of both simulation approaches, given that a low enough collision time (high enough stiffness) is used in the DEM simulations.

7.1 Model system

The system consists of a quasi-two-dimensional vibrated box with a base of variable width l_x, depth $l_y = 5d$ and infinite height, with d the diameter of the particles. The container is vibrated sinusoidally such that the position of the base is given by $b(t) = A\sin(\omega t)$, with A and ω our parameters of energy injection. Previous experimental and numerical studies have revealed a variety of non-equilibrium stable states, dependent mainly on the amount of energy injection [TMLS89, EvdWvdM$^+$07, RLT13]. Here we focus on the high energy injection limit, where a density inverted and horizontally homogeneous state is present, usually referred to as granular Leidenfrost state [EvdWvdML05]. We restrict our study to this state as it combines a high temperature gaseous state with a low temperature dense state, two adequate limits to test the micro-macro transition approaches and to compare the soft and hard MD models. Previous studies have revealed that the phase-space in this high energy limit is better

represented by the dimensionless shaking strength $S \equiv A^2\omega^2/gd$, and the number of filling layers $F \equiv Nd^2/l_x l_y$.

Collisions between particles are determined by a normal coefficient of restitution in ED simulations, $r_{ED} = 0.9$. In the DEM case we use the linear spring-dashpot model (see Eq. (3)), and set the stiffness k and viscous damping γ_0 by choosing t_c, the typical collision time, and r, the coefficient of restitution, as given by Eqs. (4) and (5). Naturally, we set $r = r_{ED}$, and t_c is left as a free parameter. Lateral walls are considered rigid and having the same collision parameters than between particles in both types of simulations.

7.2 Experimental comparison

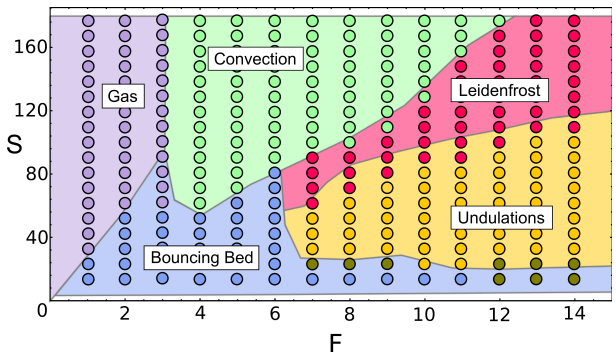

Figure 8: Phase space of the wide $l_x = 100d$ box geometry, for $A = 4.0d$ and variable ω. Circles correspond to ED simulations, while background is taken from experiments presented in [EvdWvdM$^+$07], where also the different states are carefully described.

As a first step of validation, ED simulation results are compared with previous experimental work done in a wide container [EvdWvdM$^+$07], $l_x = 100d$. In this case we account for friction with a fixed coefficient $\mu = 0.1$. The wide system presents many distinct non-homogeneous stable states in the S-F space. For a detail analysis of all states see Ref. [EvdWvdM$^+$07]. Here we remark that ED simulations are able to capture all observed behaviours, as shown in Fig. 8. Quantitatively, the phase space obtained from ED simulations shows a remarkable agreement with the experimental one, although there is a noticeable disagreement for some regions of transition. The source of these disagreements can come from many factors: different effective restitution and friction coefficients, the method for defining the different regions, as also physical relevance of effects ignored in simulations, such as interstitial air or grain-grain attractive forces.

7.3 Leidenfrost state

Having verified that ED simulations are in good agreement with physical experiments, we now turn our attention to the relation of both simulational methods, ED and DEM. The macroscopic states are compared by computing the packing fraction ϕ; the kinetic pressure $p = \mathrm{tr}(\underline{\underline{\sigma}}^k)/3$, with the kinetic stress tensor defined in (34b); and the granular temperature $T = \frac{1}{3}(\langle \vec{v}^2 \rangle - \langle \vec{v} \rangle^2)$. The system is further constrained by setting $l_x = 5.0d$, as we are only interested in studying the horizontally homogeneous Leidenfrost state. In this limit all horizontally inhomogeneous states are suppressed, including the buoyancy-driven convective states expected for higher S [RLT13]. Furthermore, we set $F = 12$ (which implies a total number of particles $N = 300$) and $A = 1.0d$.

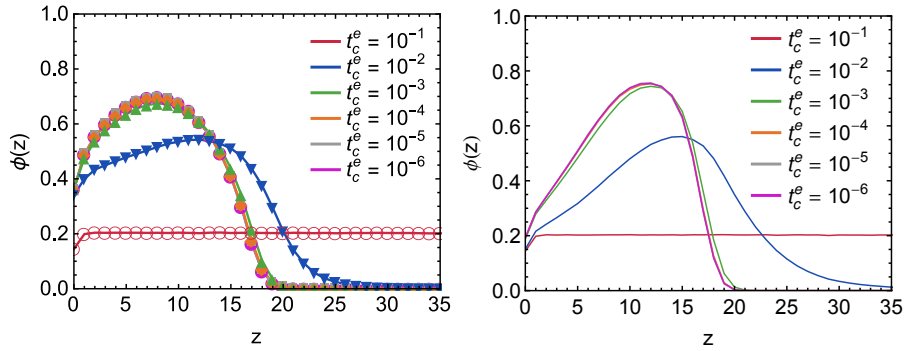

Figure 9: Time averaged packing fraction profiles $\phi(z)$ for different t_c^e, as specified in the labels, with $A = 1.0d$ and $\omega = 2.0\sqrt{g/d}$ (left), and $\omega = 5.0\sqrt{g/d}$ (right). For values of $t_c^e \leq 10^{-4}$ curves are seen to converge and are superimposed.

In ED simulations the TC model is used, both to prevent inelastic collapse and compare with the finite collision time of DEM simulations, as elaborated in Section 4. As t_c^e is reduced, the macroscopic fields converge, as shown in Figure 9 for the averaged packing fraction vertical profile, $\phi(z)$. There is no significant difference between the low and high energy injection limits, both converging for $\tau_c \sim 10^{-5}$, the value taken for the following simulations.

It is important to remark that macroscopic fields are not computed using the same procedure; it is also the purpose of the following work to see how both approaches compare. In the ED case, instantaneous macroscopic fields are obtained by coarse graining space in rectangular bins and computing the relevant quantities by averaging over the bins; after that, time-average is done for at least 10000 oscillation cycles. On the other hand, in DEM simulations the fields are obtained using the homogenization procedure described in Section 5, and with more detail in [WTLB12a]. The homogenization is done for the relevant quantities of density and momentum, from which the other fields can be directly obtained. Then, time-averaged totals can be obtained either

as an average of each instantaneous field, or from the time-averaged fields of velocity and density; in our case, we choose the latter method, except with the temperature field where both approaches are compared, as they present significant differences. In both cases, care is taken to acquire data with a sub-period resolution of $0.05T$, in order to prevent aliasing errors.

Figure 10 shows the time averaged vertical profiles $\langle\phi(z)\rangle_t$, $\langle P(z)\rangle_t$ and $\langle T(z)\rangle_t$ for both ED and DEM simulations with $S = 100$. The collision time t_c is modified in order to see how macroscopic fields depend on it. They correspond to 5, 10, to 50 times the collision time, for $t_c = 0.1$, $t_c = 0.05$ and $t_c = 0.01$, respectively.

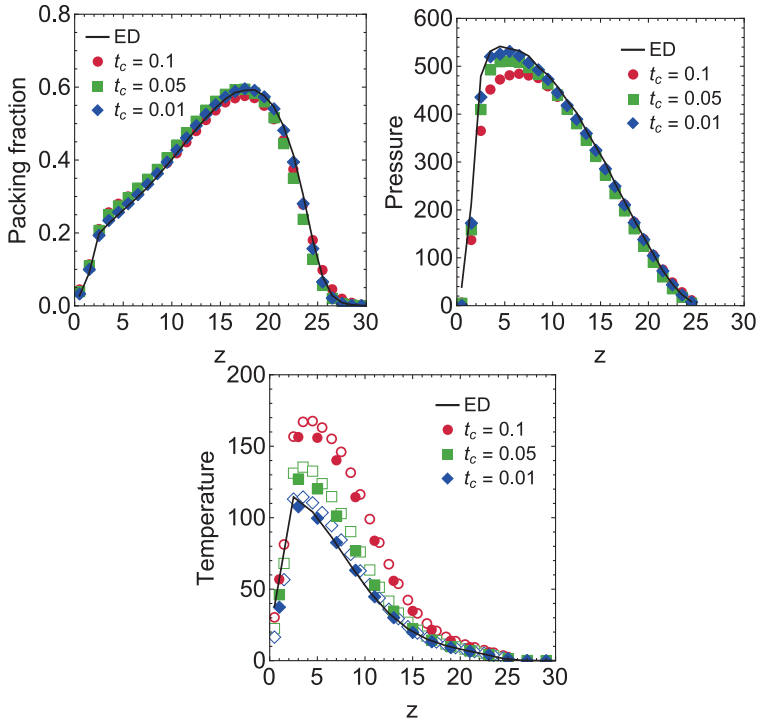

Figure 10: (a) Time averaged packing fraction vertical profiles for ED simulations (black) and soft-particle simulations with $t_c = 0.1$ (red circles), $t_c = 0.05$ (green squares) and $t_c = 0.01$ (blue diamonds). (b) Time averaged pressure vertical profiles, with the same color code. (c) Time averaged granular temperature vertical profiles, with the same color code. Open symbols corresponds to the fluctuating time-averaged velocities, while filled ones show the time-averaged fluctuating velocity, as detailed in the main text.

Remarkably, the packing fraction fields coincide to within 0.1% already for $t_c = 0.05$. The profiles are remarkably similar even for high t_c, although the effect of decreasing the collision time is considerable, specially in highly packed regions, as also near

the bottom of the container, that is, in the highly agitated region. At the bottom of the container, softer particles would over predict the time of collision with the fast moving bottom plate, and thus a low t_c is needed to approach the hard sphere limit.

The total pressure, on the other hand, presents a more pronounced difference for higher values of t_c, although there is already only a 3% disagreement between both schemes for $t_c = 0.05$. Reducing t_c further leads to a better overall agreement, although the pressure in the gaseous zone is still considerably lower than in the hard-sphere limit.

The temperature field presents a considerably higher disagreement between ED and MD simulations for higher values of t_c. This could be due to many factors. Mainly, the time-averaging of the fields in the SP case may have a big influence on a highly fluctuating quantity such as temperature. The fluctuations come mainly from the dependency on the inverse of density, which can have very low values instantly, but not in the long time average. The difference between the different time average schemes is shown in dashed and solid lines, respectively: it is clear that computing the temperature at each frame from the density and velocity fields, and then averaging over the whole simulation, leads to a better agreement for all t_c (Figure 10c). Nevertheless, both profiles always present the same overall behaviour, and the agreement is again good for $t_c = 0.001$.

7.4 Summary

In the case of collisional systems, with rather high packing fractions, ED simulations present a surprisingly good agreement with previous experiments of a highly agitated granular bed, and also agree very well with DEM simulations with rather hard particles. A low enough t_c is needed to accurately match the conserved hydrodynamic fields, especially when different time-averaging schemes play a role, such as with the granular temperature. It is important to remark that even though the density and pressure can present remarkably similar profiles for a given t_c, the corresponding temperature field can be considerably over-predicted in DEM simulations. Overall, we see that the hard-particle limit and event-driven simulations present an excellent alternative for the simulation of fluidized, yet quite dense, granular systems, usually being orders of magnitude faster than DEM simulations.

8 Discussion and Conclusion

A summary of soft particle molecular dynamics (referred to as discrete element methods (DEM) in some fields of engineering), and hard particle event-driven (ED) simulations was given. The two approaches were compared in various situations, from dilute/collisional to dense, inertial chute flows. The less dynamic, quasi-static regimes are addressed in Refs. [TML, DS]. In the dilute regime both methods are identical while in denser situations, the finite contact duration time and multi-particle contacts

become relevant. Those contacts are readily modeled in DEM, see also Ref. [Mar], but not in ED. An extension of ED involves a new time-scale over which collisions between particles are considered elastic, both to avoid the divergence of the number of collisions per unit time and to model the natural fact of finite collision times, an approach referred to as the TC (time/duration of contacts) model. An alternative simulation method is contact dynamics (CD), which was addressed in Ref. [Rad]. Furthermore, a methodology for relating the particle properties from particle simulations to the state variables and fields in continuum models has been presented, with more details and practical exercises presented in Ref. [TWT]. This micro-macro transition was defined for the density, velocity, velocity gradient, stress and temperature fields via the coarse graining approach, which ensures that mass, momentum and energy balance are exactly preserved. Additional fields like the structure tensor (fabric), couple-stress, rotations, and curvature were not considered here but are subject of ongoing research.

Given any type of particle simulation method, DEM, ED, CD or others, but also given experimental data, the coarse-graining procedure to obtain conserved fields from particle simulations depends on a critical parameter w, the length-scale of the kernel (smoothing) function. Using granular flows down an inclined plane as reference system, we have observed that the choice of w for a particular system can be justified by determining its scale-dependence, and identifying scales that are insensitive to the choice of w. Similarly, coarse-graining in time requires a similar approach with a time-scale t_w. Furthermore, an interaction force density has been introduced, that can capture the boundary conditions of the bulk flow, as well as drag relations with other constituents in a mixed flow (not shown, data to be presented elsewhere). Situations where the w- or t_w-dependence persists (in either space or time, or both) can relate to either flows with micro-structure or transients and are subject to ongoing studies. Note that the micro-macro methodology is valid, but such cases will display strong fluctuations and require further research.

Given one has a steady state situation with a w-independent plateau, one can proceed further and accumulate continuum fields with good statistics and quality from a single simulation. The methodology permits the definition of a complete (tensorial) rheological model for steady, planar non-Newtonian granular flows from particle simulations. The stress is decomposed as: *(i)* the isotropic pressure, *(ii)* the *anisotropy*, i.e., the ratio of deviatoric stress and pressure, *(iii)* the anisotropic stress distribution between the principal directions, and *(iv)* the difference in orientation of tensor eigen-systems. Using the coarse graining methodology in a chute-flow system, we have seen that the rheology deviates from a Newtonian fluid behaviour not only due to its pressure- and strain-rate-dependent viscosity (the well-known macroscopic friction referred to as the $\mu(I)$-rheology), but also has a non-trivial anisotropic stress distribution and a slight lag between the orientation of the stress and the strain rate tensor. These effects need to be taken into account for any truly quantitative prediction of granular flow behaviour; even though being small for chute flows, we expect them to be more important in other situations as, e.g., situations with strain reversal and transient regimes.

Hard-sphere, event-driven (ED) simulations were compared with both previous experimental realizations and soft-particle simulations of a highly agitated granular bed. ED simulations are able to capture the whole spectrum of behaviors observed in the quasi-two-dimensional vibrated system as the energy is increased, from low to very high energy inputs, the phase-space even presenting good quantitative agreement. The TC model, an approach to solve the inelastic collapse problem and model the softness, i.e. the finite collision times, with perfectly hard spheres, was studied in this highly agitated limit, and the parameters needed to obtain convergence were determined. In such situations, ED and DEM simulation approaches coincide remarkably well in their macroscopic fields, given that a low enough collision time is set in DEM simulations, especially for the computation of the most sensitive field: the granular temperature.

In conclusion, discrete element methods (soft or hard) are a helpful tool to understanding many granular, particulate, powder or geo-materials. The same ideas and methods can also be applied to atomistic systems [HGWL12, HTL13]. The micro-macro methods presented in this paper can be applied to both DEM and ED simulation results, but also to CD or experimental data. The overall goal to obtain micro- and particle-based constitutive relations for continuum theory has seen many success-stories but not all challenges have been addressed so far and many open questions remain. The qualitative approach of using DEM in the early years has now developed into the attempt of a quantitative predictive modelling tool for the diverse modes of complex momentum and energy transport in granular media, industrial and natural, environmental processes and phenomena. To achieve the goal of a micro-based macro-theory will remain a research challenge for the next decade, involving enhanced kinetic theories for dense collisional flows and elaborate constitutive models for quasi-static, dense systems with, e.g., shear band localisation. In the future this will allow to better understand, to better design/optimize and to impose the desired behavior, with particular applications in mind as, e.g., modern sintered materials, reactors involving catalysts, tabletting, selective laser-sintering, and many others. This concerns not only man-made processes and flows but also natural phenomena like avalanches, land-slides or civil engineering issues like slow creep or instabilities of foundations.

Acknowledgements
Special thanks to V. Richefeu for proofreading and K. Taghizadeh with helping to assemble, format, edit this and the other papers for this ALERT course. Financial support is acknowledged from NWO, STW, FOM (the Netherlands), and DFG (Germany).

References

[AT87] M. P. Allen and D. J. Tildesley. *Computer Simulation of Liquids*. Oxford University Press, Oxford, 1987.

[Bab97] M. Babic. Average balance equations for granular materials. *International Journal of Engineering Science*, 35(5):523–548, 1997.

[BSL11] M. N. Bannerman, R. Sargant, and L. Lue. DynamO: a free $o(n)$ general event-driven molecular dynamics simulator. *Journal of Computational Chemistry*, 32(15):3329–3338, November 2011.

[BUK+05] G. Bartels, T. Unger, D. Kadau, D. E. Wolf, and J. Kertesz. The effect of contact torques on porosity of cohesive powders. *Granular Matter*, 7:139, 2005.

[CR] G. Combe and J.-N. Roux. Good practice and sample preparation - construction of granular packings. *ALERT geomaterials Doctoral School 2017, Aussois, France*.

[dCEP+05] Frdric da Cruz, Sacha Emam, Michal Prochnow, Jean-Nol Roux, and Franois Chevoir. Rheophysics of dense granular materials: Discrete simulation of plane shear flows. *Physical Review E*, 72(2):021309, 2005.

[DS] F.-V. Donzé and L. Scholtés. Predicting the strength of anisotropic shale rock: empirical nonlinear failure criterion vs. Discrete Element Method. *ALERT geomaterials Doctoral School 2017, Aussois, France*.

[DvZTR05] E. Dintwa, M. van Zeebroeck, E. Tijskens, and H. Ramon. Torsion of viscoelastic spheres in contact. *Granular Matter*, 7:169, 2005.

[Els06] Danie Els. Definition of roll velocity for spherical particles. submitted, 2006.

[EvdWvdM+07] P. Eshuis, K. van der Weele, D. van der Meer, R. Bos, and D. Lohse. Phase diagram of vertically shaken granular matter. *Physics of Fluids*, 19(12):123301, 2007.

[EvdWvdML05] P. Eshuis, K. van der Weele, D. van der Meer, and D. Lohse. Granular leidenfrost effect: Experiment and theory of floating particle clusters. *Physical Review Letters*, 95(25), December 2005.

[GAC+06] C. Goldenberg, A. P. F. Atman, P. Claudin, G. Combe, and I. Goldhirsch. Scale separation in granular packings: Stress plateaus and fluctuations. *Physical Review Letters*, 96(16), 2006.

[GG01] B. J. Glasser and I. Goldhirsch. Scale dependence, correlations, and fluctuations of stresses in rapid granular flows. *Physics of Fluids*, 13(2):407–420, 2001.

[Gol10] I. Goldhirsch. Stress, stress asymmetry and couple stress: from discrete particles to continuous fields. *Granular Matter*, 12(3):239–252, 2010.

[Haf83] P. K. Haff. Grain flow as a fluid-mechanical phenomenon. *J. Fluid Mech.*, 134:401–430, 1983.

[HGWL12] Remco Hartkamp, A. Ghosh, Thomas Weinhart, and Stefan Luding. A study of the anisotropy of stress in a fluid confined in a nanochannel. *Journal of Chemical Physics*, 137(4), 2012.

[HHL98] H. J. Herrmann, J.-P. Hovi, and S. Luding, editors. *Physics of dry granular media - NATO ASI Series E 350*, Dordrecht, 1998. Kluwer Academic Publishers.

[HTL13] R. Hartkamp, B. D. Todd, and S. Luding. A constitutive framework for the non-newtonian pressure tensor of a simple fluid under planar flows. *Journal of Chemical Physics*, 138(24), 2013.

[HW04] H. Hinrichsen and D. E. Wolf. *The Physics of Granular Media*. Wiley VCH, Weinheim, Germany, 2004.

[IK50] J. H. Irving and J. G. Kirkwood. The statistical mechanical theory of transport processes .4. the equations of hydrodynamics. *Journal of Chemical Physics*, 18(6):817–829, 1950.

[IK04] I. Iordanoff and M. M. Khonsari. Granular lubrication: Toward an understanding of the transition between kinetic and quasi-fluid regime. *Journal of Tribology*, 126(1):137–145, 2004.

[JFP06] Pierre Jop, Yol Forterre, and Olivier Pouliquen. A constitutive law for dense granular flows. *Nature*, 441(7094):727–730, 2006.

[JR85] J. T. Jenkins and M. W. Richman. Kinetic theory for plane shear flows of a dense gas of identical, rough, inelastic, circular disks. *Phys. of Fluids*, 28:3485–3494, 1985.

[KBG49] J. G. Kirkwood, F. P. Buff, and M. S. Green. The statistical mechanical theory of transport processes. *J. Chem. Phys.*, 17(10):988, 1949.

[KIML13] N. Kumar, O. I. Imole, V. Magnanimo, and S. Luding. Evolution of the effective moduli for anisotropic granular materials during pure shear. In *AIP Conference Proceedings*, volume 1542, pages 1238–1241. AIP Publishing, June 2013.

[Kis01] Y. Kishino, editor. *Powders & Grains 2001*, Rotterdam, 2001. Balkema.

[KLM14] N. Kumar, S. Luding, and V. Magnanimo. Macroscopic model with anisotropy based on micro-macro information. *Acta Mechanica*, 225:2319–2343, 2014.

[KOL14] Dinant Krijgsman, Vitaliy Ogarko, and Stefan Luding. Optimal parameters for a hierarchical grid data structure for contact detection

in arbitrarily polydisperse particle systems. *Computational Particle Mechanics*, 1(3):357–372, 2014.

[LAM11] Stefan Luding and Fernando Alonso-Marroquin. The critical-state yield stress (termination locus) of adhesive powders from a single numerical experiment. *Granular Matter*, 13(2):109–119, 2011.

[LCB+94a] S. Luding, E. Clément, A. Blumen, J. Rajchenbach, and J. Duran. Anomalous energy dissipation in molecular dynamics simulations of grains: The "detachment effect". *Phys. Rev. E*, 50:4113, 1994.

[LCB+94b] S. Luding, E. Clément, A. Blumen, J. Rajchenbach, and J. Duran. The onset of convection in molecular dynamics simulations of grains. *Phys. Rev. E*, 50:R1762, 1994.

[LCRD96] S. Luding, E. Clément, J. Rajchenbach, and J. Duran. Simulations of pattern formation in vibrated granular media. *Europhys. Lett.*, 36(4):247–252, 1996.

[LG03] S. Luding and A. Goldshtein. Collisional cooling with multi-particle interactions. *Granular Matter*, 5(3):159–163, 2003.

[LH99] S. Luding and H. J. Herrmann. Cluster growth in freely cooling granular media. *Chaos*, 9(3):673–681, 1999.

[LHMZ98] S. Luding, M. Huthmann, S. McNamara, and A. Zippelius. Homogeneous cooling of rough dissipative particles: Theory and simulations. *Phys. Rev. E*, 58:3416–3425, 1998.

[LLH01] S. Luding, M. Lätzel, and H. J. Herrmann. From discrete element simulations towards a continuum description of particulate solids. In A. Levy and H. Kalman, editors, *Handbook of Conveying and Handling of Particulate Solids*, pages 39–44, Amsterdam, The Netherlands, 2001. Elsevier.

[LM98] S. Luding and S. McNamara. How to handle the inelastic collapse of a dissipative hard-sphere gas with the TC model. *Granular Matter*, 1(3):113–128, 1998. e-print cond-mat/9810009.

[LMM05] S. Luding, K. Manetsberger, and J. Muellers. A discrete model for long time sintering. *Journal of the Mechanics and Physics of Solids*, 53(2):455–491, 2005.

[Lub91] B. D. Lubachevsky. How to simulate billards and similar systems. *J. Comp. Phys.*, 94(2):255, 1991.

[Lub92] B. D. Lubachevsky. Simulating billiards: Serially and in parallel. *Int.J. in Computer Simulation*, 2:373–411, 1992.

[Lud97] S. Luding. Surface waves and pattern formation in vibrated granular

media. In *Powders & Grains 97*, pages 373–376, Amsterdam, 1997. Balkema.

[Lud98] S. Luding. Collisions & contacts between two particles. In H. J. Herrmann, J.-P. Hovi, and S. Luding, editors, *Physics of dry granular media - NATO ASI Series E350*, page 285, Dordrecht, 1998. Kluwer Academic Publishers.

[Lud06] S. Luding. About contact force-laws for cohesive frictional materials in 2d and 3d. In P. Walzel, S. Linz, Ch. Krülle, and R. Grochowski, editors, *Behavior of Granular Media*, pages 137–147. Shaker Verlag, 2006. Band 9, Schriftenreihe Mechanische Verfahrenstechnik, ISBN 3-8322-5524-9.

[Lud07] S. Luding. Contact models for very loose granular materials. In Peter Eberhard, editor, *Symposium on Multiscale Problems in Multibody System Contacts*, pages 135–150. Springer, 2007. ISBN 978-1-4020-5980-3.

[Lud08] S. Luding. Cohesive frictional powders: Contact models for tension. *Granular Matter*, 10:235–246, 2008.

[Lud09] Stefan Luding. Towards dense, realistic granular media in 2d. *Nonlinearity*, 22(12):R101, 2009.

[Mar] C.L. Martin. Advanced contact laws. *ALERT geomaterials Doctoral School 2017, Aussois, France*.

[MiD04] GDR MiDi. On dense granular flows. *The European Physical Journal E*, 14(4):341–365, 2004.

[Mil04] S. Miller. *Clusterbildung in granularen Gasen*. PhD thesis, Universität Stuttgart, 2004.

[ML04a] S. Miller and S. Luding. Cluster growth in two- and three-dimensional granular gases. *Phys. Rev. E*, 69:031305, 2004.

[ML04b] S. Miller and S. Luding. Event driven simulations in parallel. *J. Comp. Phys.*, 193(1):306–316, 2004.

[MY94] S. McNamara and W. R. Young. Inelastic collapse in two dimensions. *Phys. Rev. E*, 50(1):R28–R31, 1994.

[OL13] Vitaliy Ogarko and Stefan Luding. Prediction of polydisperse hard-sphere mixture behavior using tridisperse systems. *Soft Matter*, 9:9530–9534, 2013.

[PL01] T. Pöschel and S. Luding, editors. *Granular Gases*, Berlin, 2001. Springer. Lecture Notes in Physics 564.

[Rad] F. Radjai. The contact dynamics (CD) method. *ALERT geomaterials Doctoral School 2017, Aussois, France*.

[Rap95] D. C. Rapaport. *The Art of Molecular Dynamics Simulation*. Cambridge University Press, Cambridge, 1995.

[RLT13] N. Rivas, S. Luding, and A. R. Thornton. Low-frequency oscillations in narrow vibrated granular systems. *New Journal of Physics*, 15(11):113043, November 2013.

[SML15] A. Singh, V. Magnanimo, and S. Luding. Mesoscale contact models for sticky particles. *arXiv:1503.03720*, 2015.

[SMSL14] Abhinendra Singh, Vanessa Magnanimo, Kuniyasu Saitoh, and Stefan Luding. Effect of cohesion on shear banding in quasistatic granular materials. *Phys. Rev. E*, 90:022202, Aug 2014.

[STS93] M. H. Sadd, Q. M. Tai, and A. Shukla. Contact law effects on wave propagation in particulate materials using distinct element modeling. *Int. J. Non-Linear Mechanics*, 28(2):251, 1993.

[TCC17] Colin Thornton, Sharen J. Cummins, and Paul W. Cleary. On elastic-plastic normal contact force models, with and without adhesion. *Powder Technology*, 315:339 – 346, 2017.

[TED95] B. D. Todd, D. J. Evans, and P. J. Daivis. Pressure tensor for inhomogeneous fluids. *Physical Review E*, 52(2):1627–1638, 1995.

[TKdV+13] A.R. Thornton, D. Krijgsman, A. de Voortwis, O. Orgarko, S. Luding, R. Fransen, S. Gonzalez, O. Bokhove, O. Imole, and T Weinhart. A review of recent work on the discrete particle method at the university of twente: An introduction to the open- source package mercurydpm. In *Discrete Element Methods 6*, 2013.

[TKF+13] Anthony Thornton, Dinant Krijgsman, Rudi Fransen, Sebastian Gonzalez, Deepak Tunuguntla, Ate ten Voortwis, Stefan Luding, Onno Bokhove, and Thomas Weinhart. Mercury-dpm: Fast particle simulations in complex geometries. *EnginSoft Newsletter*, 10(1), 2013.

[TML] K. Taghizadeh, S. Luding, and V. Magnanimo. DEM applied to soil mechanics. *ALERT geomaterials Doctoral School 2017, Aussois, France*.

[TMLS89] B. Thomas, M. O. Mason, Y. A. Liu, and A. M. Squires. Identifying states in shallow vibrated beds. *Powder Technology*, 57(4):267–280, April 1989.

[Tom00] Jürgen Tomas. Particle adhesion fundamentals and bulk powder consolidation. *KONA*, 18:157–169, 2000.

[TWLB12a] A. R. Thornton, T. Weinhart, S. Luding, and O. Bokhove. Frictional dependence of shallow-granular flows from discrete particle simulations. *Eur Phys J E Soft Matter*, 35(12):9804, 2012.

[TWLB12b] Anthony Thornton, Thomas Weinhart, Stefan Luding, and Onno Bokhove. Modeling of particle size segregation: calibration using the discrete particle method. *International Journal of Modern Physics C*, 23(8), 2012.

[TWOL13] Anthony Thornton, Thomas Weinhart, Vitaliy Ogarko, and Stefan Luding. Multiscale modeling of multi-component granular materials. *Computer Methods in Materials Science*, 13:197–212, 2013.

[TWT] D. Tunuguntla, T. Weinhart, and A. Thornton. Discrete particle simulations with MercuryDPM. *ALERT geomaterials Doctoral School 2017, Aussois, France*.

[VDE+01] P. A. Vermeer, S. Diebels, W. Ehlers, H. J. Herrmann, S. Luding, and E. Ramm, editors. *Continuous and Discontinuous Modelling of Cohesive Frictional Materials*, Berlin, 2001. Springer. Lecture Notes in Physics 568.

[VL16] Dalila Vescovi and Stefan Luding. Merging fluid and solid granular behavior. *Soft Matter*, 12:8616–8628, 2016. arXiv:1609.07414.

[WAD95] Eligiusz Wajnryb, Andrzej R. Altenberger, and John S. Dahler. Uniqueness of the microscopic stress tensor. *The Journal of Chemical Physics*, 103(22):9782–9787, 1995.

[WB86] O. R. Walton and R. L. Braun. Viscosity, granular-temperature, and stress calculations for shearing assemblies of inelastic, frictional disks. *J. Rheol.*, 30(5):949–980, 1986.

[WHTL13] Thomas Weinhart, Remco Hartkamp, Anthony R. Thornton, and Stefan Luding. Coarse-grained local and objective continuum description of three-dimensional granular flows down an inclined surface. *Physics of Fluids*, 25(7), 2013.

[WLT13] Thomas Weinhart, Stefan Luding, and Anthony R. Thornton. From discrete particles to continuum fields in mixtures. In *AIP Conference Proceedings*, volume 1542, pages 1202–1205. AIP Publishing, 2013.

[WTLB12a] Thomas Weinhart, Anthony R. Thornton, Stefan Luding, and Onno Bokhove. Closure relations for shallow granular flows from particle simulations. *Granular Matter*, 14(4):531–552, 2012.

[WTLB12b] Thomas Weinhart, Anthony R. Thornton, Stefan Luding, and Onno Bokhove. From discrete particles to continuum fields near a boundary. *Granular Matter*, 14(2):289–294, 2012.

[ZSS91] C. Y. Zhu, A. Shukla, and M. H. Sadd. Prediction of dynamic contact loads in granular assemblies. *J. of Applied Mechanics*, 58:341, 1991.